

THESIS FOR THE DEGREE OF DOCTOR OF PHILOSOPHY

Thin-Film Coated Steel Foils as Interconnects for Solid Oxide
Fuel Cells (SOFC)

Oxidation and Chromium Evaporation Properties

Rakshith Nugehalli Sachitanand



CHALMERS

Department of Chemistry and Chemical Engineering

CHALMERS UNIVERSITY OF TECHNOLOGY

Gothenburg, Sweden 2015

Thin-Film Coated Steel Foils as Interconnects for Solid Oxide Fuel Cells (SOFC)
Oxidation and Chromium Evaporation Properties

RAKSHITH NUGEHALLI SACHITANAND
ISBN: 978-91-7597-250-3

© Rakshith Nugehalli Sachitanand, 2015.

Doktorsavhandlingar vid Chalmers tekniska högskola
Ny serie nr 3931
ISSN nr 0346-718X

Department of Chemistry and Chemical Engineering
Division of Energy and Materials
Chalmers University of Technology
SE-412 96 Gothenburg
Sweden
Telephone + 46 (0)31-772 1000

Cover:

Bright field STEM micrograph of the oxide scale grown on the Ce/Co-coated sample at 850°C in air+3% H₂O with a total flow rate of 6000sml/min (Sead Canovic).

Chalmers Reproservice AB
Gothenburg, Sweden 2015

Abstract

Solid Oxide Fuel Cells (SOFCs) are high-temperature ($>600^{\circ}\text{C}$) electrochemical energy conversion devices that can operate on a broad range of fuels while achieving efficiencies exceeding that of state of the art heat engines. The advancement of the technology has however been hindered by a number of technical and economic barriers, one of which is the durability and cost of the bipolar plate or interconnect that connects individual cells in series to form a so-called 'stack'.

The ferritic steel based interconnect experiences oxidising ($p(\text{O}_2) \approx 0.2$ bar) and reducing ($p(\text{O}_2) < 10^{-15}$ bar) conditions on its 'air' and 'fuel' sides respectively. In air side environments, the chromium rich oxide scale volatilises and deposits on the cathode, significantly degrading cell performance. In addition, the interconnect itself can experience accelerated degradation due to the extraneous loss of Cr resulting from the volatilisation process.

This thesis focusses primarily on the Cr evaporation and oxidation properties of uncoated and PVD coated ferritic steel foils in air side environments at 850°C . X-ray diffraction (XRD), Scanning Electron Microscopy (SEM) and Transmission Electron Microscopy (TEM) coupled with Energy Dispersive X-ray (EDX) analysis have been used to investigate oxidation mechanisms and establish a quantitative framework to evaluate the influence of coatings on the oxidation of the interconnect material.

It is shown using long term experiments (>3000 h) that the application of a 10nm thick layer of Ce on the steel surface significantly improves the oxidation resistance of the steel while time resolved Cr evaporation data establishes the fact that a 640nm thick Co coating reduces the evaporation rate by one order of magnitude in air side environments. A duplex coating consisting of 10nm of Ce underneath 640nm of Co successfully minimises both the oxidation and evaporation rate.

Additionally, the effect of PVD coatings on the oxidation performance of interconnects in simulated fuel side environments are examined. It is established that Ce and La coatings brings about a factor 2-3 reduction in the oxidation rate. The presence of a La coating results in the formation of a continuous perovskite layer by reaction with the thermally grown oxide; a property that could be leveraged to improve the otherwise poor conductivity of the oxide scale in low oxygen partial pressure environments.

List of Publications

The thesis is based on the following papers, referred to by Roman numerals in the text. The papers are appended at the end of the thesis.

Paper I

R. Sachitanand, M. Sattari, J.E. Svensson and J. Froitzheim

Evaluation of the oxidation and Cr evaporation properties of selected FeCr alloys used as SOFC interconnects. *International Journal of Hydrogen Energy*, **38**:15328-15334 (2013).

Paper II

R. Sachitanand, J. E. Svensson and J. Froitzheim

The Influence of Cr Evaporation on Long Term Cr Depletion Rates in Ferritic Stainless Steels. *Oxidation of Metals*, Published Online (2015).

Paper III

S. Canovic, J. Froitzheim, R. Sachitanand, M. Nikumaa, M. Halvarsson, LG Johansson and J.E. Svensson

Oxidation of Co- and Ce-nanocoated FeCr steels: A microstructural investigation. *Surface and Coatings Technology*, **215**:62-74 (2013).

Paper IV

M. Sattari, R. Sachitanand, J. Froitzheim, J.E. Svensson and T. Jonsson

The effect of Ce on the high temperature oxidation properties of a Fe–22%Cr steel: microstructural investigation and EELS analysis. *Materials at High Temperatures*, **32**:118-122 (2015).

Paper V

R.Sachitanand, S.Canovic, J.E. Svensson and J. Froitzheim

On the Lifetime of Coated Ferritic Steels used as SOFC interconnects. Manuscript.

Paper VI

R. Sachitanand, M. Sattari, J.E. Svensson and J. Froitzheim

Coatings for SOFC Interconnects in Fuel Side Environments. Accepted, *Fuel Cells* (2015).

Statement of author's contribution

I was the main author in papers I, II, V and VI In papers III and IV, I performed the experiments and assisted in describing the experimental setup.

The TEM analysis in paper III was performed by Sead Canovic. Mohammad Sattari performed the microanalysis in papers IV and VI.

Related work

I have made a contribution to the following paper, which is extensively referenced to in the text:

[43] J. Froitzheim, S. Canovic, M. Nikumaa, R. Sachitanand, L.G. Johansson, J.E. Svensson

Long term study of Cr evaporation and high temperature corrosion behaviour of Co coated ferritic steel for solid oxide fuel cell interconnects, *Journal of Power Sources*, **220**:217-227 (2012)

Table of Contents

Abstract	i
List of Publications.....	ii
Statement of author's contribution	iv
Related work.....	iv
1. Introduction.....	1
2. Aim	2
3. Oxidation theory	3
3.1. Oxide formation and thermodynamics	7
3.1.1. Oxide formation.....	7
3.1.2. Oxidation kinetics.....	7
3.2. Cr evaporation	10
4. Fuel cells	13
4.1. Introduction.....	13
4.2. Solid Oxide Fuel Cells	15
4.2.1. Electrolyte	15
4.2.2. Cathode	16
4.2.3. Anode	16
4.2.4. Seals.....	17
4.2.5. Interconnects	17
5. Experimental techniques	20
5.1. Experimental Setup	20
5.1.1. Air Side Experiments	20
5.1.2. Fuel Side Experiments.....	21
5.2. Sample Preparation.....	21
6. Analytical techniques.....	22

6.1. Scanning Electron Microscopy (SEM)	22
6.2. Spectrophotometry	23
6.3. Transmission Electron Microscopy (TEM)	24
6.4. X-ray Diffraction (XRD).....	25
7. Results and Discussion	27
7.1. A comparison of the oxidation properties of uncoated interconnect steels in air+3% H ₂ O at 850°C	27
7.2. The Oxidation and Cr Evaporation Properties of Coated and Uncoated Sanergy HT up to 1000 h	30
7.3. Oxide Scale Development on Coated and Uncoated Sanergy HT in air+3% H ₂ O at 850°C up to 1000 h	32
7.3.1. The uncoated steel	32
7.3.2. Ce 10nm Coating	34
7.3.3. Co 640nm Coating.....	35
7.3.4. Co 640nm / Ce 10nm Coating.....	37
7.4. The Oxidation and Cr evaporation Properties of Coated and Uncoated Sanergy HT beyond 1000 h	38
7.5. Oxide Scale Development on Coated and Uncoated Sanergy HT in air+3% H ₂ O at 850°C beyond 1000 h.....	39
7.5.1. The uncoated steel	39
7.5.2. Ce 10nm Coating	40
7.5.3. Co 640nm Coating	41
7.5.4. Co 640nm / Ce 10nm Coating.....	41
8. Estimation of the chemical lifetime of the coated and uncoated interconnect in cathode side environments.....	43
8.1. Quantifying the Impact of Coatings on Cr depletion	43
9. Oxidation of Coated and Uncoated Interconnect materials in Ar-5% H ₂ +3% H ₂ O at 850°C.....	52

10. Conclusion 57

11. Outlook 59

12. Acknowledgements..... 61

13. References 62

1. Introduction

A planet stretched for resources drives the need for newer fuels and energy conversion technologies. Solid Oxide Fuel Cells (SOFCs) are high temperature electrochemical energy conversion devices that have the potential to deliver high chemical to electrical energy efficiencies, using a wide variety of fuels (1, 2). While promising much, the state of the art SOFC is still plagued by a number of technological issues.

An SOFC consists of three main components: an anode, an electrolyte and a cathode. In order to achieve sufficient voltage, several cells are connected in series using bipolar plates also known as interconnects. The ideal SOFC interconnect must meet various specific, at times even contradictory requirements such as high temperature oxidation resistance and high electronic conductivity. In addition to this, the interconnect must have mechanical properties that are compatible with other cell components. Different materials have been suggested for use as SOFC interconnects (1, 2). Stainless steels have emerged as ideal candidates because of the balance between cost and performance that they offer (3-5).

At the relatively high operating temperatures of an SOFC (650-1000°C), the air side of the interconnect experiences rapid oxidation and simultaneous volatilisation of the protective chromia scale that forms on its surface during operation. The repercussions of this volatilisation process are twofold: degradation in cell performance due to poisoning of the cathode (6-8) and shortened material lifetimes due to the accelerated depletion of Cr in the steel.

Two approaches exist for combating the related but separate issues of Cr evaporation and rapid oxidation. The first; changing the alloy composition has achieved some success (4, 5, 9) but, crucially, the issue of Cr evaporation has not been resolved through this route. Additionally, finding a suitable alloy composition that resists high temperature corrosion on both the air and fuel sides is extremely difficult. The second approach, using coatings to tailor the surface properties of the individual sides of the interconnect introduces the possibility to attack the problem where it is prevalent without having to compromise on the alloy bulk properties.

2. Aim

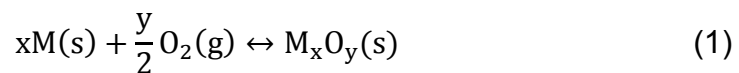
This work aims to:

- a) Investigate the mechanisms of oxide growth on coated and uncoated ferritic steel based interconnect materials in SOFC relevant environments.
- b) Quantify the impact of Cr evaporation on the oxidation performance of ferritic steels developed for SOFC interconnect applications and evaluate the effect of coatings on Cr evaporation and high temperature oxidation behaviour.

3. Oxidation theory

Most metals are thermodynamically unstable in oxygen containing environments (10, 11). Temperature is an important parameter as it greatly influences the rate of reaction. For corrosion resistance, alloys rely on the formation of a well adherent, protective oxide scale on their surface.

The oxidation reaction of a metal M with oxygen gas O₂ can be written as in Equation 1.



The second law of thermodynamics is used to determine whether or not a reaction can occur. It can be written in terms of the Gibbs free energy (G) for the system:

$$G = H - TS \quad (2)$$

Most high temperature oxidation processes occur at constant temperature and pressure. For closed systems at constant pressure, the following statements are valid regarding the free energy change (ΔG) associated with a process (12):

At equilibrium:

$$\Delta G = 0 \quad (3)$$

For a spontaneous process (disregarding activation energy):

$$\Delta G < 0 \quad (4)$$

For an endergonic (energy consuming) process

$$\Delta G > 0 \quad (5)$$

For the chemical reaction



The Gibbs free energy change (ΔG) may be expressed as

$$\Delta G = \Delta G^\circ + RT \ln \left(\frac{a_C^c a_D^d}{a_A^a a_B^b} \right) \quad (7)$$

where ΔG° is the free energy change when all the species are in their standard states, a is the thermodynamic activity of a substance which represents its effective concentration under non-ideal conditions and can be approximated in terms of partial pressures as

$$a_i = \frac{p_i}{p_i^\circ} \quad (8)$$

where p_i is the partial pressure of a gaseous species (i) and p_i° represents its partial pressure in the standard state (usually 25°C and 1 atm). The Equation assumes ideal gas behaviour and relatively low pressures.

The standard free energy change for such a system can then be written as

$$\Delta G^\circ = c\Delta G^\circ_C + d\Delta G^\circ_D - a\Delta G^\circ_A - b\Delta G^\circ_B \quad (9)$$

When the system is at equilibrium, the equation for ΔG reduces to

$$\Delta G^\circ = -RT \ln \left(\frac{a_C^c a_D^d}{a_A^a a_B^b} \right) \quad (10)$$

where the quantity in brackets in Equation 10 represents the equilibrium constant for the reaction described in Equation 6.

$$K_{eq} = \left(\frac{a_C^c a_D^d}{a_A^a a_B^b} \right) \quad (11)$$

For the reaction of the tetravalent metal M with $O_2(g)$:



The equilibrium constant described in Equation 11 can be written as:

$$K_{eq} = \left(\frac{a_{MO_2}}{a_M a_{O_2}} \right) \quad (13)$$

If the activities of the metal and its oxide are approximated to unity, the partial pressure of oxygen at which the metal and its oxide are in equilibrium can be readily derived:

$$p_{O_2}^{M/MO_2} = e^{\frac{\Delta G^o}{RT}} \quad (14)$$

A plot of the standard gibbs free energy of formation vs temperature, known as the Ellingham diagram, is commonly used to compare the relative thermodynamic stabilities of metal-oxide systems under both oxidising and reducing conditions (see Figure 1)

However, when considering alloys, the activities of the metal and its oxide are not unity and must thus be taken into account:

$$p_{O_2}^{eq} = \frac{a_{MO_2}}{a_M} e^{\frac{\Delta G^o}{RT}} \quad (15)$$

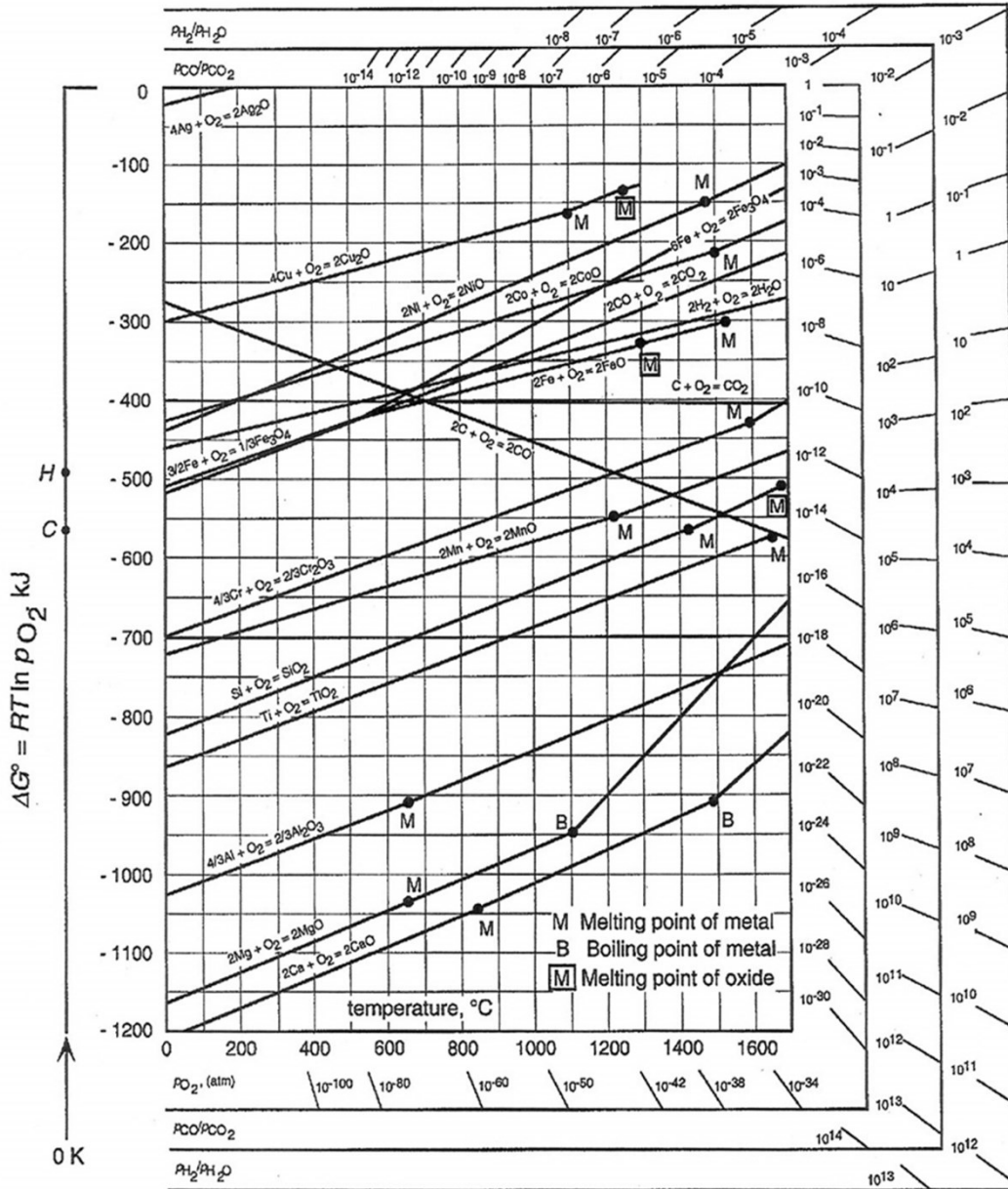


Figure 1 Ellingham diagram for selected oxides (10)

3.1. Oxide formation and thermodynamics

3.1.1. Oxide formation

The initial oxidation process at high temperatures can be divided into three major steps (Figure 2) (11)

- The adsorption and dissociation of $O_2(g)$ from the environment onto the metal surface, followed by charge transfer and O^{2-} formation
- Oxide nucleation and lateral growth to form a continuous scale
- Further growth in a direction normal to the substrate surface.

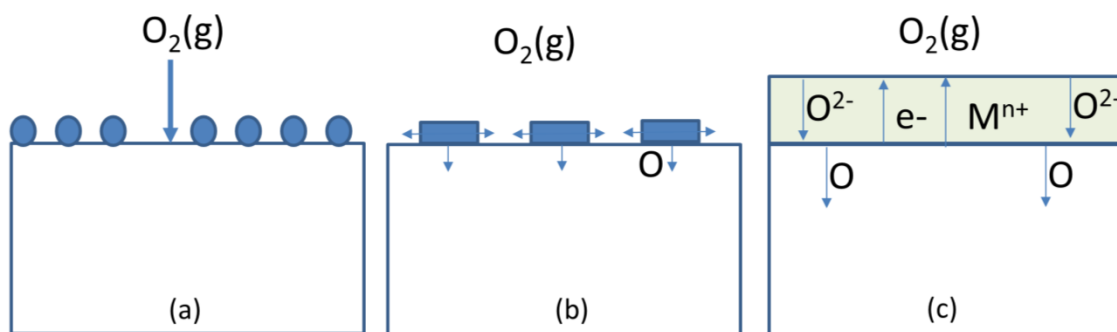


Figure 2 Schematic diagram showing the major steps of the high temperature oxidation process based on Kofstad (11)

Steps (a) and (b) occur rapidly where the surface reactions are rate controlling. The completion of step (b) results in the formation of a continuous oxide film on the surface. Step (c) proceeds via solid-state diffusion of either or both the anions (oxidant) and cations (metal ions) through the scale. The diffusion process through the scale then becomes the rate determining step. This process is strongly temperature dependant; at room temperatures, the growth rate is negligible while at higher temperatures, it is significantly fast.

3.1.2. Oxidation kinetics

While thermodynamic equilibrium drives the corrosion process, reaction kinetics often dictate the scale growth and formation characteristics. Oxidation kinetics are commonly determined using gravimetric analysis and described by linear, parabolic or logarithmic models of growth. In reality however, considerable deviation exists from these models and the resulting reaction kinetics are usually a combination of the aforementioned models.

3.1.2.1. *Linear rate law*

During linear growth, the oxidation rate is constant with respect to time and is independent of the amount of metal or gas previously consumed. The rate-determining step is usually either a surface reaction or a phase boundary reaction (10). The linear oxidation kinetic is visible during the very initial stages of oxidation, prior to the formation of an oxide scale or when the rate determining step occurs at the scale gas interface. Linear growth can be described by the equation:

$$\frac{dx}{dt} = k \quad (16)$$

or

$$x = k \times t \quad (17)$$

where x is scale thickness and t is time, assuming that no scale has been formed at $t=0$

3.1.2.2. *Parabolic rate law*

If the metal-oxide and oxide-gas interfaces are in thermodynamic equilibrium, the oxide growth rate is typically dominated by either the inward transport of oxygen ions or the outward transport of metal ions. A process involving ionic transport requires the simultaneous transport of electrons in order to maintain the charge balance. Ionic species can be transported via the oxide lattice and/or oxide grain boundaries (11).

A simplified treatment of the derivation of the parabolic rate law is presented below, assuming outward cation flux to be the rate controlling step. An analogous derivation can also be made assuming inward anion transport to be the dominant process.

The outward flux of cations is assumed to be equal and opposite to the flux of cation vacancies:

$$j_{M^{+}} = -j_{V''_M} = D_{V''_M} \frac{C_{V''_M}^2 - C_{V''_M}^1}{x} \quad (18)$$

where $j_{M^{+}}$ represents the outward flux of cations, $j_{V''_M}$ represents the inward flux of cation vacancies and $(C_{V''_M}^2 - C_{V''_M}^1)$ is the difference in metal-ion vacancy concentration between the scale-gas and metal-oxide interfaces respectively. The

quantity x represents the thickness of the metal oxide while $D_{V''_M}$ represents the diffusion coefficient for metal-ion vacancies through the oxide film (see Figure 3).

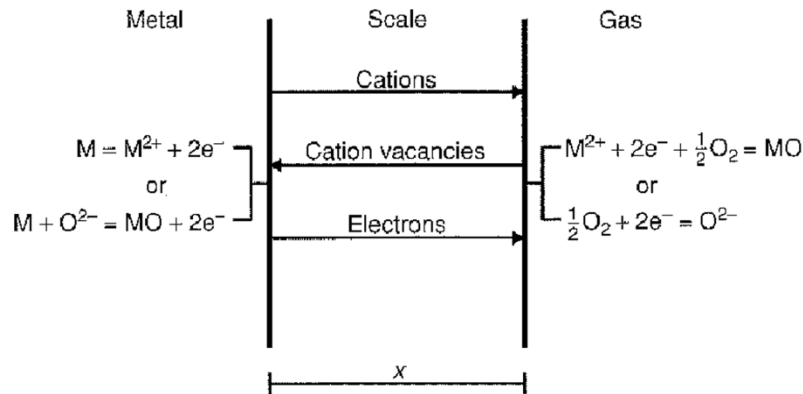


Figure 3 Simplified model of cation diffusion controlled high temperature oxidation(10)

Since the quantity $C_{V''_M}^2 - C_{V''_M}^1$ is a constant when the metal-oxide and oxide-gas interfaces are at equilibrium, the outward metal flux $j_{M\cdot}$ can be written as:

$$j_{M\cdot} = \frac{1}{V_{ox}} \frac{dx}{dt} = D_{V''_M} \frac{C_{V''_M}^2 - C_{V''_M}^1}{x} = \frac{k'}{x} \quad (19)$$

where V_{ox} is the molar volume of the oxide and $k_p = D_{V''_M} (C_{V''_M}^2 - C_{V''_M}^1)$. For $x=0$ at $t=0$, the integrated form of Equation 19 yields:

$$x^2 = 2k't \quad (20)$$

This shows that the thickness increases as a square root of time t . The constant k' is proportional to the diffusivity of the rate-controlling ionic species. As the oxide scale thickens, the diffusion distance increases causing the reaction rate to decline over time.

3.1.2.3. *Logarithmic law*

The logarithmic kinetic is said to be applicable at lower temperatures, usually between 300 and 400°C and is characterised by rapid initial growth followed by very slow continued growth (10).

$$\frac{dx}{dt} = \frac{1}{t + t_0} \quad (21)$$

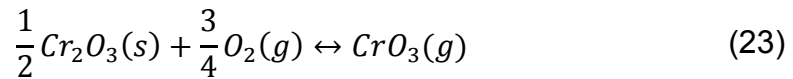
Or

$$x = k \log(t + t_0) \quad (22)$$

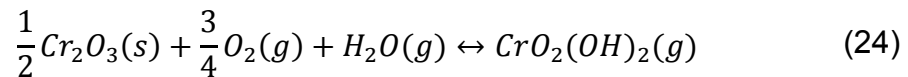
The change in the reaction rate from rapid to an almost passive behaviour is attributed to the difference between the adsorbed oxygen fraction (α) on a clean metal surface contra the quantity adsorbed when that surface has been covered by a thin monolayer of oxide. As the surface becomes completely covered with oxide, it exhibits an almost passive behaviour which is visible after longer exposure times.

3.2. Cr evaporation

The formation of Cr(g) is thermodynamically allowed at high temperatures, but in the presence of oxygen, this is prevented by the formation of a passive oxide, and instead, the surface of the Cr rich oxide scale is volatilised in the presence of O₂ to form CrO₃(g) according to Equation 23



In the presence of water vapour, the attack is accelerated by the formation of oxyhydroxides of Cr:



Tedmon (13) proposed a kinetic model that incorporated the effect of Cr evaporation into mass gain data and suggested a so called parilinear growth kinetic. He assumed that in pure O₂, CrO₃ evaporated at a constant rate k_s , whose value depended on experimental conditions. The oxide is assumed to continue to grow according to parabolic rate kinetics. The equation describing the rate of oxide scale thickening is thus modified to

$$\frac{dx}{dt} = \frac{k_d}{x} - k_s \quad (25)$$

where k_d is one half of the parabolic rate constant. The growth kinetic is characterised by the kinetic competition between ionic diffusion through the oxide scale and the

evaporation of Cr from the oxide surface. An increase in oxide thickness is observed, when oxide growth is faster than the evaporation rate. A plot of the gravimetrically determined mass gain over time accordingly exhibits a positive slope. As the oxide scale thickens further, the growth rate of the oxide slows to eventually equal that of oxide loss through volatilisation. This is observed experimentally as the point when the slope of the mass gain curve tends to zero. Beyond this point, a steady state is maintained wherein the oxide thickness remains constant due to the equality between oxide growth rate and oxide loss rate. However, a negative mass gain is recorded over time due to the loss of Cr via evaporation. This is illustrated qualitatively in Figure 4. Ebbinghaus (14) performed thermodynamic calculations based on the available experimental data for Cr evaporation in dry O_2 and O_2+H_2O and concluded that CrO_3 was the dominating evaporation product in dry O_2 while $CrO_2(OH)_2$ dominated in O_2+H_2O . The validity of these results was verified by Opila et al (15). The gas flow rate has a bearing on the rate of Cr evaporation (16, 17) . This is illustrated in Figure 5 (16) where the evaporation rate from a 22%Cr steel is plotted against the gas flow rate in an environment consisting of air+3% H_2O at $850^\circ C$. At lower flow rates, a linear region is observed where the evaporation reaction is in the equilibrium regime. As the flow rate increases a plateau is encountered (around 25 cm/s in Figure 5) where the evaporation reaction becomes flow rate independent. At this stage, the kinetics are steered by the formation of $CrO_2(OH)_2$.

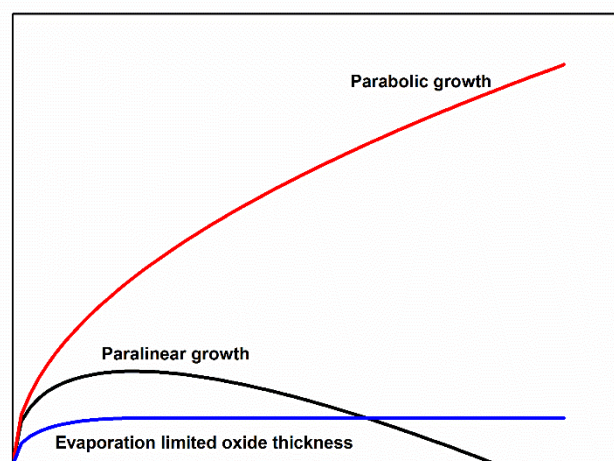


Figure 4 A qualitative visualisation of the effect of Cr evaporation on mass gain and oxide thickness over time, based on (18)

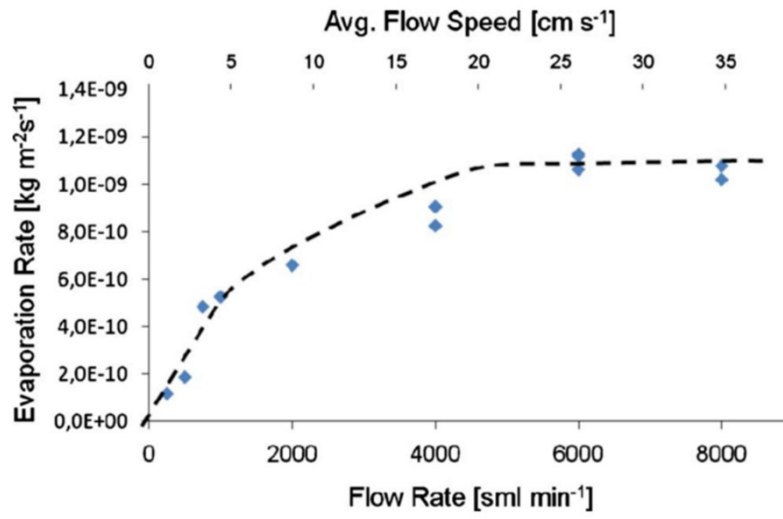


Figure 5 The effect of gas flow rate on Cr evaporation from a 22% Cr steel at 850°C in air+3% H₂O (16)

4. Fuel cells

4.1. Introduction

A fuel cell is an electrochemical energy conversion device that converts chemical energy to electricity. A fuel cells construction can be likened to that of a battery, but in contrast the fuel cell continuously converts chemical energy to electricity whereas a battery stores chemical energy and discharges it when connected to an external circuit. The basic components of a fuel cell are:

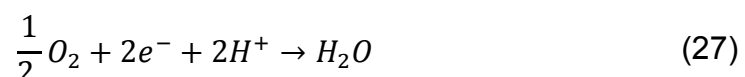
- I) Anode
- II) Electrolyte
- III) Cathode

For all fuel cells, the electrolyte acts as a membrane that separates the anode from the cathode. In the simplest form of a fuel cell, the oxidant present on the cathode side consists of O_2 while the fuel on the anode side consists of H_2 . A membrane or electrolyte separates the oxidant from the fuel. When the cathode and anode are connected via an external circuit, the concentration gradient across the electrolyte drives an electrochemical reaction that involves the ionic diffusion of either the anionic or cationic species across the electrolyte membrane coupled with electronic conduction or a current, via an external circuit in order to maintain the charge balance. The half-cell reactions for a proton conducting fuel cell where H_2 is the fuel are as follows:

Anode:



Cathode:



When the fuel cell has an oxide ion conducting membrane, such as in an SOFC, the half-cell reactions are given in Equations (28) and (29).

Anode:



Cathode:



A schematic diagram showing the basic layout of a proton fuel cell is shown in Figure 6 and a similar diagram for an oxide-ion-conducting cell, such as an SOFC, is illustrated in Figure 7.

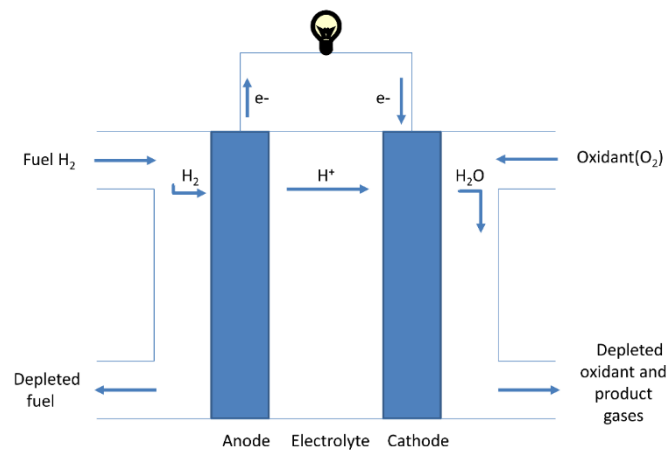


Figure 6 A schematic diagram of a proton conducting fuel cell

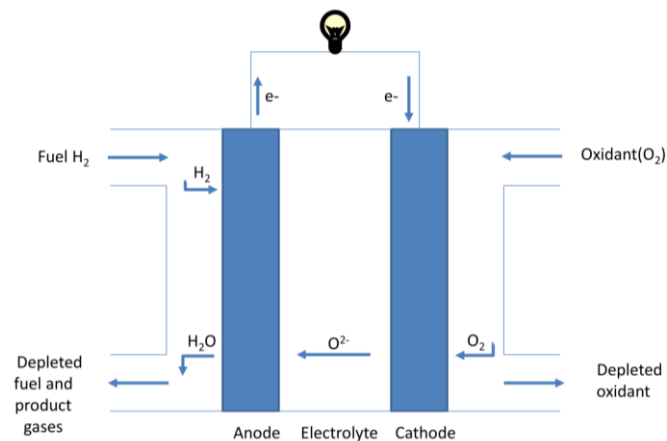


Figure 7 A schematic diagram of an oxide ion conducting fuel cell (SOFC)

4.2. Solid Oxide Fuel Cells

Solid oxide fuel cells have an all solid design and operate at higher temperatures than other fuel cells which are required for the oxygen ion conductivity in the solid electrolyte. This has several advantages; the higher temperatures bring the ability to use fuels apart from hydrogen because of the potential for internal reformation and provide independence from precious metal catalysts. Additionally, the higher temperatures also provide high quality waste heat that can be used for power generation downstream of the stack (1). The solid electrolyte construction eliminates the need for complicated electrolyte management as is the case with other types of fuel cells. The high temperatures, however, bring with them some disadvantages such as thermal stresses generated by the large temperature difference between the stack and its surrounding. This calls for careful matching of the thermal expansion coefficient of the various stack components; a thermal expansion coefficient mismatch could cause damage to the stack during heating and cooling (19)



Figure 8 Press photo of a 500 kW SOFC system manufactured by Bloom Energy and installed at an eBay data center. The systems are run on biogas and provide uninterrupted power to the server farms, utilising the electricity grid as a backup (20).

4.2.1. Electrolyte

The most popular electrolyte material for a solid oxide fuel cell is yttrium stabilised zirconia (YSZ), where the Y concentration varies between 8-10 wt%. The Y doping leads to a replacement of Zr^{4+} ions by Y^{3+} ions and in the process, stabilises the cubic phase. The charge balance requirement leads to an increase in oxygen vacancies and

thus increased oxygen ion conductivity. Since O^{2-} diffusion is a solid state process, it requires high temperatures (above $700^{\circ}C$) to achieve meaningful performance levels. One way to improve the ionic conductivity of YSZ at intermediate temperatures is to dope it with Sc (1). Other materials such as Gd doped CeO_2 or perovskite structured materials have also been investigated as potential electrolyte materials but the most widespread is still YSZ (1, 21).

4.2.2. Cathode

The cathode of an SOFC must fulfil a number of requirements: It must be electronically conductive, chemically and dimensionally stable during fabrication, minimally reactive with the electrolyte and interconnect and be highly catalytically active for O_2 dissociation and oxygen reduction. The cathode must also be as porous as possible to allow oxygen to reach the cathode-electrolyte interface.

Lanthanum Manganite ($LaMnO_3$) is the most common SOFC cathode material. It is often doped with Sr (typically around $La_{0.8}Sr_{0.2}MnO_3$ abbreviated to LSM) to produce the required electronic conductivity. Higher conductivity can result from higher dopant levels but this negatively affects the thermal expansion coefficient. The triple phase boundary (region where cathode, oxygen and electrolyte meet) is often enhanced by mixing in YSZ at a 50/50 ratio prior to sintering. In this way, a thicker triple phase boundary can be formed which reduces the cathodes contribution to cell resistance. However, at lower temperatures ($600-750^{\circ}C$) LSM suffers from low oxygen ion conductivity and is therefore replaced with $(La,Sr)(Co,Fe)O_3$ (LSCF) (1, 2, 21)

4.2.3. Anode

The anode must be an excellent catalyst for the oxidation of the fuel. In addition to this, it must be electronically conductive, possess compatible thermal expansion properties, be chemically stable in the fuel environment and be sufficiently porous to allow the gas to diffuse to the anode-electrolyte interface. Initially, precious metals such as Pt and Au and transition metals such as Ni and Fe were tested (1, 21) but were found to be unsuitable. Ni, for instance, is an excellent catalyst but possesses a thermal expansion coefficient that is too high and coarsens due to sintering at high temperatures. Ni-YSZ cermets are currently the material of choice for SOFC anodes due to their lower thermal expansion coefficient and their ability to prevent the sintering of Ni (1). Ni has the dual role of catalysing fuel oxidation in addition to being a current collector. Nickel

is also active in the steam reforming of methane, a property which allows fuel cells to operate on different mixtures of methane and water. However, a high steam-to-carbon ratio must be maintained to prevent the formation of elemental carbon which leads to catalytic poisoning (1).

4.2.4. Seals

Seals are critical to the proper functioning of a SOFC stack in that they prevent the mixing of the fuel and oxidant gases within the stack while also preventing leakage out of the stack to the ambient environment. A seal must be thermochemically stable in its environment, electrically insulating, compatible thermal expansion properties and have the ability to withstand thermal cycling between the ambient and operating temperature. Examples include rigid, bonded seals (e.g. glass-ceramics), compressive seals (e.g. mica based composites) and compliant seals (e.g. viscous glasses) (2).

4.2.5. Interconnects

The interconnect (or bipolar plate) fulfils two key functions: It provides electrical contact between adjacent cells while separating the air side of one cell from the fuel side of the other. The interconnect material must possess the following properties in order to be suitable for use:

1. High electronic conductivity with low ionic conductivity
2. Chemical stability in anode and cathode side environments
3. Thermal expansion compatibility with other components
4. Ease of fabrication

Lanthanum Chromite (LaCrO_3) was a popular interconnect when SOFCs were operated around 1000°C , but with the trend towards lower operating temperatures, (below 900°C), it has been replaced with ferritic steels which offer the following advantages (i) improved manufacturability, (ii) lower raw material and manufacturing costs and (iii) higher electrical and thermal conductivity. In order to survive in an SOFC environment, certain requirements specific to this class of materials must be fulfilled. One of the most important is high temperature corrosion resistance in both air and fuel side environments. This is normally achieved by the formation of a slow growing, protective oxide layer. In addition to this, the oxide formed must hinder electronic

conduction through the interconnect as little as possible while also possessing good chemical compatibility with the electrodes.

Ferritic steels for interconnect applications can be roughly classified into two categories: (1) low Si steels that contain no Nb; these steels are generally more expensive to manufacture and require special vacuum melting practices. (2) Steels with higher quantities of Si combined with significant additions of Nb; the addition of Nb causes the formation of Laves phase (Fe_2Nb) precipitates that tie up the Si and thus minimise the formation of SiO_2 at the metal-oxide interface (4). A higher tolerance for Si results in lower manufacturing costs by allowing a shift to more conventional production techniques (4). The compositions of five ferritic-steel based interconnect materials (weight %) are presented in Table 1.

Name	Manufacturer	Fe	Cr	Mn	Si	W/Mo	Nb	Cu	RE
E-brite	ATI Allegheny Ludlum	Bal	26	0.08	0.20	0.87Mo	0.12	-	-
ZMG232 G10	Hitachi Metals	Bal	23.7	0.28	0.02	1.4W		0.93	0.07La/0.28Zr
Sanergy HT	Sandvik Materials Technology	Bal	21.2	0.3	0.12	0.96 Mo	0.71	-	0.24Zr
Crofer 22 H	ThyssenKrupp VDM	Bal	22.7	0.42	0.2	1.4 W	0.55	-	0,08La
Crofer 22 APU	ThyssenKrupp VDM	Bal	22.7	0.48	0.02	-	-	-	0,09La

Table 1 Compositions in wt% of 5 ferritic steels developed for use as SOFC interconnects

Crofer 22 APU (ThyssenKrupp VDM) and ZMG232 G10 (Hitachi Metals) have low Si contents and the latter also has about 1 wt% Cu (22). Sanergy HT (16) (Sandvik Materials Technology AB) and Crofer 22 H (ThyssenKrupp VDM) (4) are Laves phase forming alloys with Nb/Si ratios of 5.9 and 1.25 respectively while the alloy E-Brite (ATI Allegheny Ludlum) stands out for its low Mn and higher (26%) Cr content in addition to an Nb/Si ratio of 0.5. A detailed discussion of the effects of Nb, W, and Si in Fe-22Cr steels can be found e.g. in (4, 23-25).

While ferritic steels are widely used, certain key performance barriers exist to their long-term stability. On the air side, Cr_2O_3 formed as a protective scale on the surface of the steel is known to volatilise to Cr(VI) species (17) and deposit on the electrode and electrolyte surfaces and interfaces. This causes a rapid decline in the oxygen

reduction capability of the cathode and a degradation in cell performance. The evaporation of Cr is usually prevented by the application of coatings. One approach is to apply a spinel or perovskite layer onto the steel surface prior to the operation. Another approach is to apply metallic coatings that react to form the protective oxide when the stack is heated up for the first time.

On the fuel side, Ni interdiffusion between the interconnect and anode leads to the formation of Austenite at the interconnect-anode interface (26, 27). The difference in thermal expansion coefficient between the austenite and the other components of the SOFC can cause cracking during heating or cooling of the stack.

5. Experimental techniques

5.1. Experimental Setup

5.1.1. Air Side Experiments

The experiments were carried out at 850°C in a horizontal quartz tube reactor (Figure 9). Two types of experiments were performed. First, the samples were exposed in a still environment that was saturated in Cr species by placing several sheets of steel in the furnace hot zone in order to minimise any evaporation reactions that might otherwise have occurred. The second environment consisted of a flowing gas where the flow rate was sufficiently high to ensure that the Cr evaporation rate was independent of gas flow rate (16). The gas composition consisted of air that was humidified with 3 vol% H₂O using a bubbling flask-condenser arrangement at a total flow rate of 6000 ml/min corresponding to an average gas velocity of 27 cm/s. A porous SiC flow restrictor was placed upstream (10mm) of the samples in order to minimize natural convection and to obtain a more uniform flow pattern. Gravimetric measurements were made using a six-decimal Sartorius balance. The steel sheets were cut into 15x15mm square coupons. With the exception of E-brite in Paper I, all samples were 0.2 mm thick.

A number of methods exist to collect Cr vapours such as transpiration techniques and condensation on ceramic plates, silicon wafers or quartz wool (28) The chromium evaporation measurement setup utilised in this work consisted of a quartz denuder tube coated with Na₂CO₃ placed at the reactor outlet. The CrO₂(OH)₂ vapours formed via the volatilisation process reacted with the Na₂CO₃ to form Na₂CrO₄ according to Equation 30:

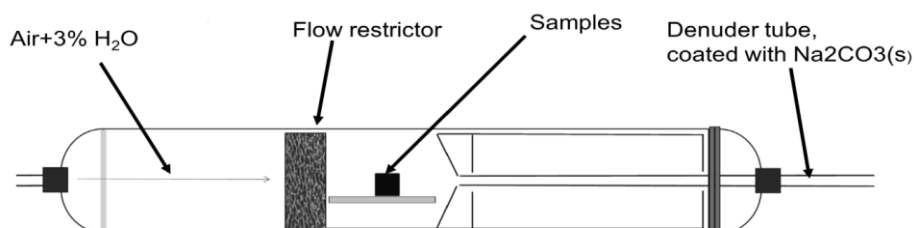
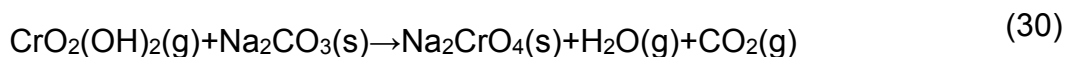


Figure 9 Schematic diagram of the experimental setup

The denuder was subsequently leached with deionized water. The Cr content in the solution was then quantified using a spectrophotometer. The collection efficiency of the denuder process is $95 \pm 5\%$ (16) .

5.1.2. Fuel Side Experiments

The experimental setup consisted of an alumina tubular reactor connected to a condenser- flask arrangement to humidify the gas. A mixture of Ar-5% H₂ (100 ml/min) was bubbled through water at 24.4°C to achieve an oxygen partial pressure of 10⁻¹⁸ bar, and subsequently allowed into the tubular reactor. The system was first leak tested and then flushed with the exposure gas for 6 h before undergoing a controlled temperature ramp at 15°C/min up to the exposure temperature of 850°C. The samples were cooled to room temperature in the exposure atmosphere and weighed periodically over the total exposure duration.

5.2. Sample Preparation

The exposures were performed on samples in an as-received state; i.e. no surface pre-treatment was carried out prior to exposure except for a degreasing and cleaning step in acetone and ethanol using an ultrasonic bath. The investigated coatings were applied prior to the cleaning steps at Sandvik Materials Technology AB using a proprietary PVD process.

6. Analytical techniques

In studying corrosion behaviour, various analytical techniques are often combined to produce data that fully describe the sample. If crystallographic information about the oxide scale is of interest, XRD is usually a good option. SEM/EDX analysis can provide elemental information about the viewed surface which can either be the top surface of the sample or a cross section through the sample to reveal the elemental composition of the various oxide layers. In short, different analytical techniques are complementary and judicious use of a combination of them is often required to study the corrosion behaviour of materials.

6.1. Scanning Electron Microscopy (SEM)

A Scanning Electron Microscope is an instrument that scans the surface of a specimen with a finely focussed electron beam. The beam produces several different sorts of signals that are measured to produce data about the area of interest. The signals can produce information about topography, atomic number, elemental composition and structure. The most commonly used signals arise from secondary electrons (SE), backscattered electrons (BSE) and X-rays (Figure 10)Figure 2. These signals escape from a certain specimen volume, known as the interaction volume. The size and shape of the interaction volume depends on the atomic number/numbers of the analysed surface.

Inelastic collisions between the beam electrons and atoms in the specimen result in the ejection of loosely bound outer shell electrons from the atom. These electrons are known as secondary electrons and possess low kinetic energies (around 50eV). If the secondary electrons are formed at a depth greater than around 10nm, they get captured by an ionised atom and fail to escape the specimen volume. If on the other hand they are formed at a depth less than 10nm, they leave the sample volume and enter the vacuum chamber where they can be detected. Secondary electrons thus provide topographical information relating to the sample surface. The topographical contrast emanates from the fact that edges produce more SEs than flat surfaces.

Backscattered electrons originate from the electron beam itself. The electrons undergo elastic collisions with the atoms in the sample. The number of backscattered electrons,

or the electron yield, is proportional to the size of the atomic nucleus. Heavier elements thus produce brighter images than lighter ones. Consequently, BSE images produce compositional contrast.

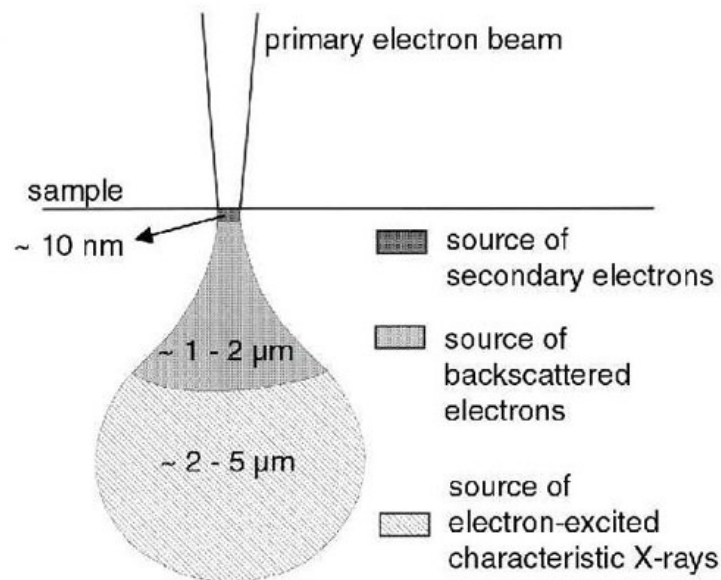


Figure 10 Schematic diagram showing the interaction volume of the electron beam with the sample and the regions of electron and X-ray generation. Image taken from (29)

X-ray generation is a two-step process. First, an electron in a lower energy orbital of a sample atom is knocked out by an atom from the electron beam. A relaxation then occurs in which an outer shell electron loses energy as an X-ray and falls to a lower energy state. The energy loss and thus the X-ray produced is characteristic for a specific element and allows for elemental identification (30).

Microanalysis during the course of this study was performed in a LEO Ultra 55 FEG SEM equipped with an Oxford Instruments Energy Dispersive X-ray spectrometer (EDX) system for chemical analysis. An acceleration voltage of 20kV and a working distance of 10mm were used for all analyses.

6.2. Spectrophotometry

A spectrophotometer consists of two parts: A spectrometer to produce light of a given wavelength and a photometer to measure the intensity of the light. A cuvette containing ions in solution is placed between these two parts. A portion of the light is absorbed and the rest is transmitted through to the photometer. The light incident on the photometer generates a voltage, the intensity of which depends on the concentration

of the ions in solution. This scheme is illustrated in Figure 11. If the concentration is linked to the intensity of colour of the solution, it is possible to make a link between absorption and ionic concentration.

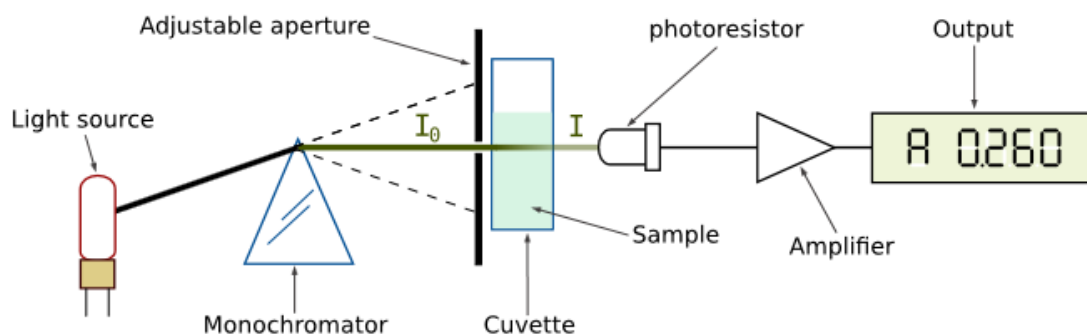


Figure 11 Essential parts of a spectrophotometer (31)

When monochromatic light passes through the solution, the Beer-Lambert law (Equation 31) can be used to determine the concentration of the ions in solution:

$$A = \log_{10} \frac{I_0}{I} \quad (31)$$

Where A is the absorbance, I_0 is the intensity of the transmitted light for a given wavelength using the pure solvent and I is the intensity of transmitted light through solution (32).

CrO_4^{2-} ions in water solution collected from Cr evaporation measurements were quantified using a Fischer Scientific Evolution 60s UV-Vis spectrophotometer equipped with a Xenon flash Lamp light source set to produce monochromatic light with a wavelength of 380 nm.

6.3. Transmission Electron Microscopy (TEM)

In Transmission Electron Microscopy, the electrons are accelerated towards the sample, much like in the SEM. The difference in this case is that, unlike in the SEM the electrons pass through the sample. For this to occur the sample must be electron transparent; this is usually the case for samples under 100 nm in thickness. In a TEM, the whole image is formed simultaneously. The acceleration voltage is significantly higher, of the order of 200 kV compared to around 20 kV for an SEM.

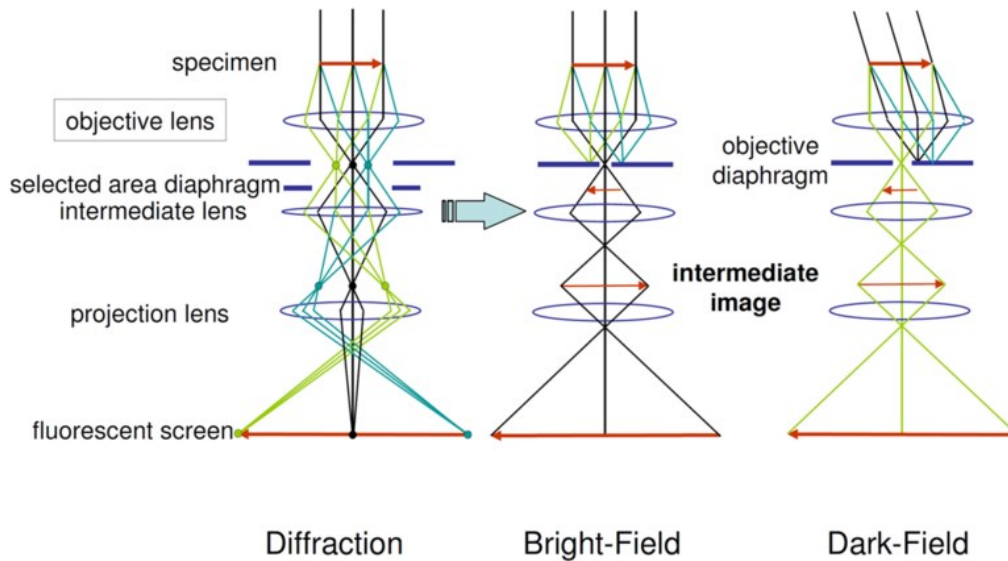


Figure 12 TEM ray paths in the diffraction (left), bright field (centre) and dark field (right) modes (33)

The TEM can be used to acquire information about the chemical composition and crystal structure with high spatial resolution. If the investigated material is crystalline, the incoming electrons will be scattered according to Bragg's law. The diffraction pattern thus arising can be used to identify the crystal structure of the studied material. The effect of diffraction can additionally be used for imaging. By using the appropriate apertures, Bright Field images (BF) composed of transmitted electrons and Dark Field images (DF), consisting of only diffracted electrons can be obtained (34).

6.4. X-ray Diffraction (XRD)

X-rays are short wavelength, high energy electromagnetic radiation. X-ray diffraction can be used to identify the various crystalline phases present in a material and is based on the constructive interference of monochromatic X-rays. When an X-ray is incident on a target material, it interacts with the electrons associated with its atoms. If the material is periodically patterned as in the case of a crystalline material, the diffracted X-rays undergo constructive interference and produce sharp interference maxima in a manner reflective of the crystalline symmetry. The occurrence of constructive interference is dependent on the wavelength of the X-ray (λ), the scattering angle (θ), the atomic plane spacing (d) and the integer (n) representing the order of the diffraction peak. This is described by Bragg's law as shown in Equation 32.

$$n\lambda = 2d \sin \theta \quad (32)$$

The principle of diffraction according to Bragg's law is schematically illustrated in Figure 13 (35).

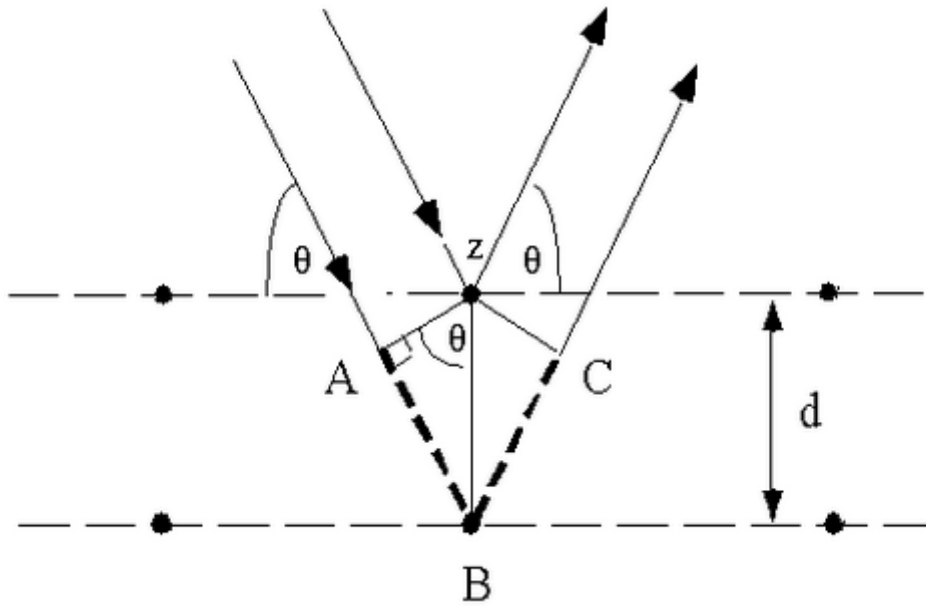


Figure 13 Schematic illustration of diffraction from neighbouring crystal planes according to Bragg's law

7. Results and Discussion

7.1. A comparison of the oxidation properties of uncoated interconnect steels in air+3% H₂O at 850°C

A number of different ferritic steel based interconnect alloys exist and Table 1 lists five such steels along with their compositions (see Section 4.2.5). In order to evaluate their relative oxidation performance, the five steels were exposed in a typical cathode side environment over 1000h. From Figure 14, it appeared that the alloy E-brite showed a mass loss while Crofer 22 APU had the highest mass gain. Time resolved Cr evaporation measurements performed on the five steels (Figure 15) show that increasing Mn alloy contents resulted in a reduction in the overall Cr evaporation rate. The alloy E-brite with almost no Mn in the steel matrix resulted in a factor 4 higher evaporation rate than the steel Crofer22 APU which contains 0.4 wt% Mn. It is thus evident that the amount of evaporated Cr is progressively reduced with increasing Mn content (Paper I).

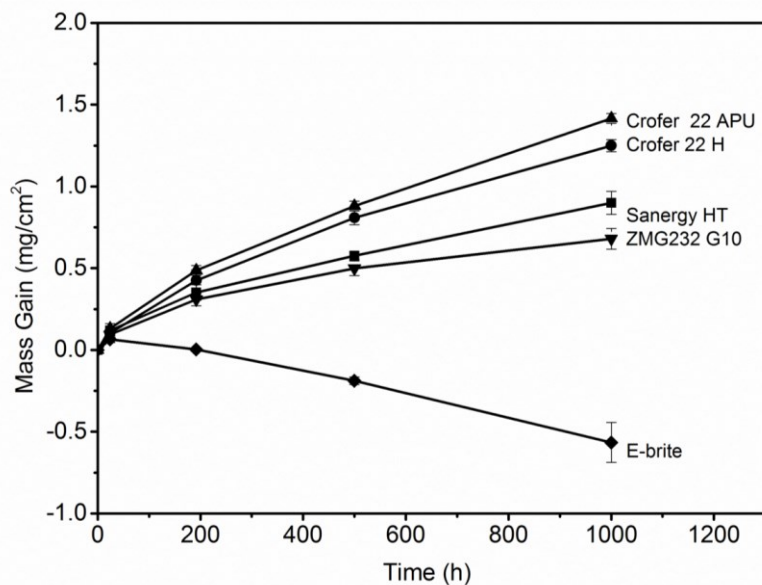


Figure 14 Discontinuous gravimetric measurements for the selected steels in air+3% H₂O at 850°C with a total flow of 6000 sml/min

With the available Cr evaporation data it is possible to calculate the mass loss due to Cr evaporation, and subsequently correct the mass gain data for this material loss. Thus, every mg of Cr lost from the oxide scale results in an equivalent loss of 1.46 mg of Cr₂O₃. Given the linearity of the Cr evaporation process over longer exposure

durations, it seems reasonable that an estimate of the mass loss due to Cr evaporation after 1000h can be estimated by doubling the value obtained experimentally after 500h. The Cr evaporation corrected mass gain curves (referred to here as the gross mass gain, Figure 16) for the studied steels over 1000h show that for the steel E-brite, while some spallation was observed the mass loss is due in large part to Cr evaporation (the dashed lines in Figure 16 represent the gravimetrically measured mass gains for the two extreme cases: E-Brite and Crofer 22 APU). The Cr evaporation corrected mass gain after 1000h was estimated to be +0.55 mg/cm² instead of -0.56 mg/cm²; a difference of 1 mg/cm². The difference between the corrected and uncorrected mass gain for Crofer 22 APU is only 0.25 mg/cm². This further demonstrates the effect of the Cr-Mn spinel on Cr evaporation behaviour.

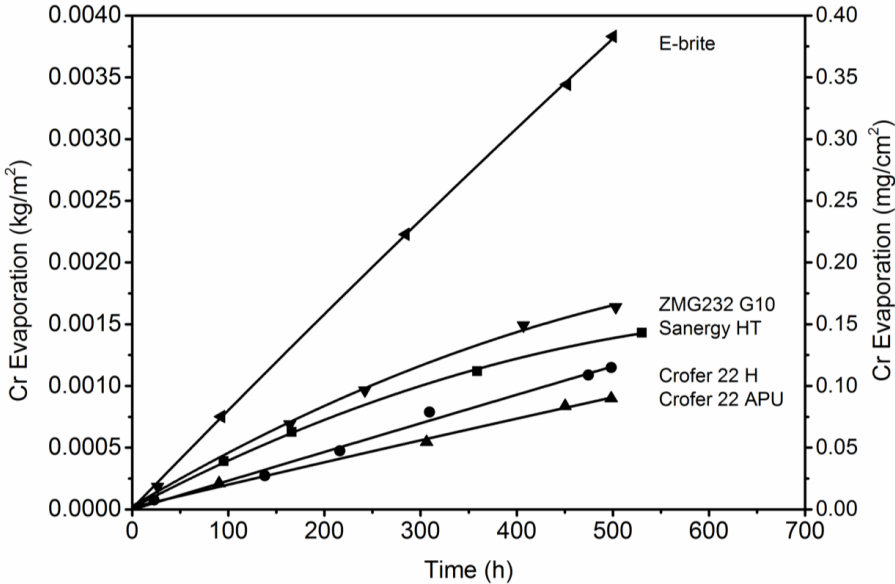


Figure 15 Time resolved Cr evaporation measurements for 5 different interconnect steels over 1000h of exposure at 850°C in air+3% H₂O and a total flow rate of 6000 sml/min

If parabolic curves are compared to Cr corrected mass gain data (dotted red lines in Figure 16), it can be observed that the Cr corrected or gross mass gain is somewhat faster than that predicted by the parabolic curves. This is explained by the fact that the scale is thinner in reality than if no evaporation had taken place, resulting in a shorter diffusion path through the oxide. The thinning due to evaporation therefore keeps the oxidation rate above what is to be expected from perfectly parabolic growth.

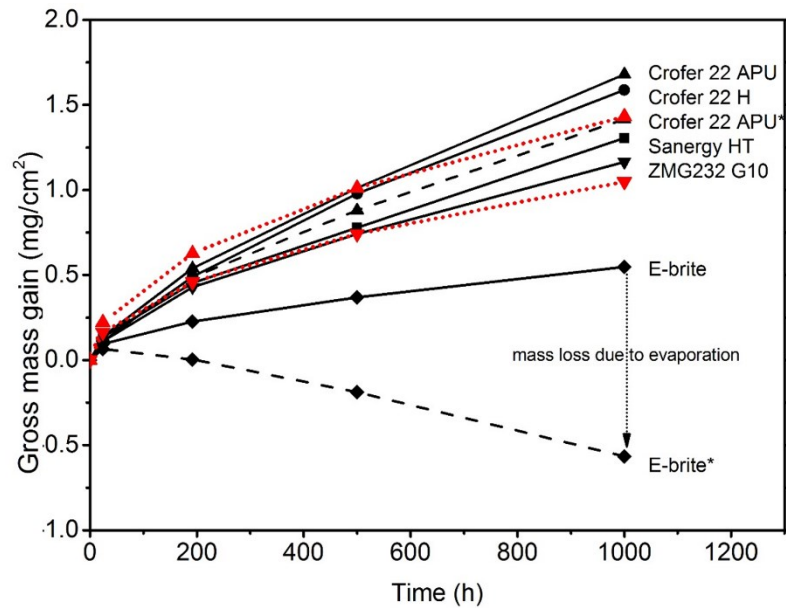


Figure 16 Gross mass gain at 850°C in air+3% H₂O for the analysed steels. The dashed lines represent net mass gain as measured by gravimetry only for the steels Crofer 22 APU and E-Brite. These lines are marked by an asterisk (*) in the legend. The dotted red lines represent parabolic fits to mass gain data for the respective steels

If the evaporation reaction is suppressed by saturating the exposure atmosphere with volatile Cr species and reducing the flow rate to near stagnant conditions (see Section 5.1.1), a parabolic mass gain curve results (marked 'no-flow' A-C mass gain in Figure 17). A comparison between the mass gain curve for the steel in stagnant, Cr vapour saturated conditions and the total oxygen uptake (gross mass gain) observed in an environment where the evaporation rate is flow-independent (compare curve A-C and A-D in Figure 17) indicates that undefined flow rates in oxidation experiments could lead to erroneous conclusions regarding the oxidation rate of the steel (Paper II).

In conclusion, Sanergy HT, while showing slightly higher Cr evaporation, was determined to be a suitable candidate for further studies on the effect of coatings. A time resolved study of the oxidation of Sanergy HT, henceforth referred to as the 'uncoated steel' and the effect of coatings on its Cr evaporation and oxidation properties is presented in the following section.

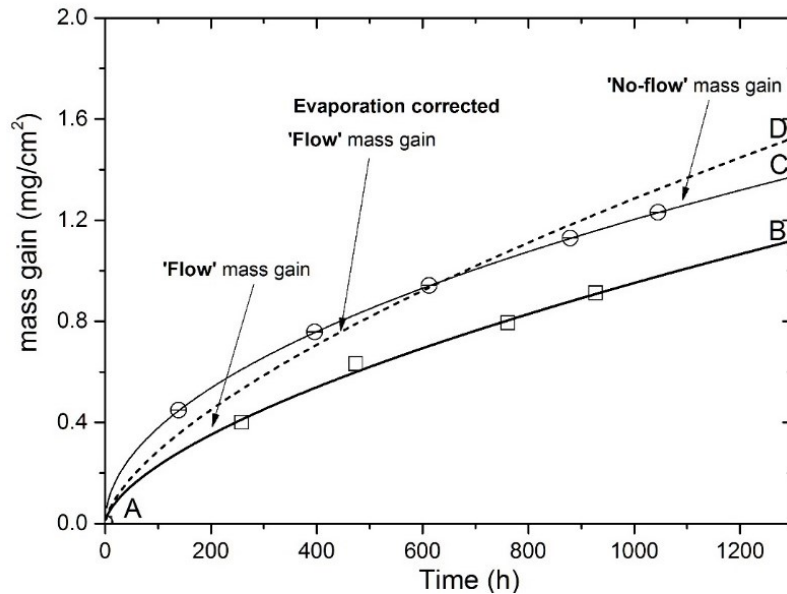


Figure 17 A comparison of oxidation data for the steel Sanergy HT exposed at at 850°C in (A-B) air+3% H₂O at 6000 sml/min (net flow mass gain), (A-C) 850°C in air saturated with volatile species of Cr ('no flow' mass gain. (A-D) represents the extent of oxygen uptake if the mass gain data in the flow condition (A-B) is corrected for Cr evaporation (gross 'flow' mass gain)

7.2. The Oxidation and Cr Evaporation Properties of Coated and Uncoated Sanergy HT up to 1000 h

Extensive work has been performed on the effect of so-called reactive elements on the oxidation properties of steels at high temperatures e.g. (36-42). Minor additions either via direct alloying or as coatings have been shown to significantly improve oxidation performance. Further, interconnect materials are often coated with Co to minimise Cr evaporation (see Section 4.2.5). It is then of interest to know how reactive elements and Co coatings effect the oxidation and Cr evaporation properties of the steel. The following investigation focusses on the effect of Ce and Co coatings on the oxidation and Cr evaporation properties of the steel, first up to 1000 h of exposure and then to longer exposure times (see Section 7.4).

The gravimetrically measured oxygen uptake or 'net mass gain' is lower when a coating of Ce is applied than when no Ce coating is present (Figure 18, compare uncoated-Ce 10nm and Co 640nm-Co 640nm/Ce 10nm respectively). When a Co coating is present, an initial higher oxidation rate is observed which is attributed to the oxidation of the Co coating to its spinel type oxide (43).

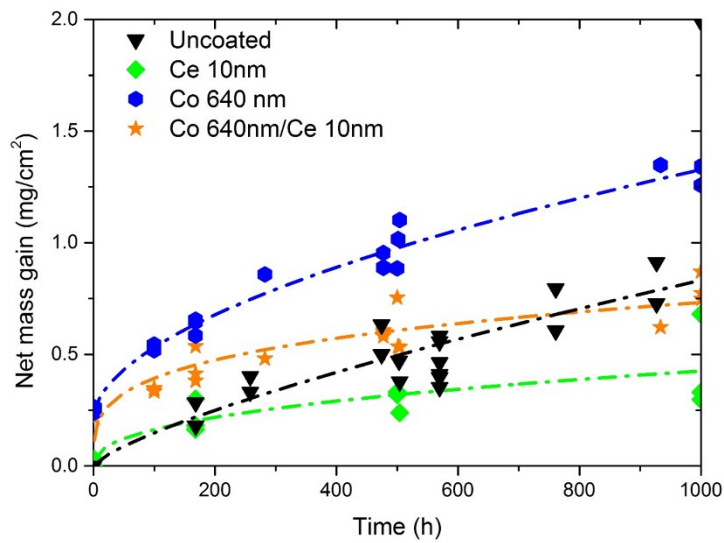


Figure 18 A comparison of net mass gain data for Sanergy HT coated with Ce, Co and Co/Ce exposed at 850 °C in air+3% H₂O with a total flow of 6000 sml/min up to a total exposure duration of 1000 h

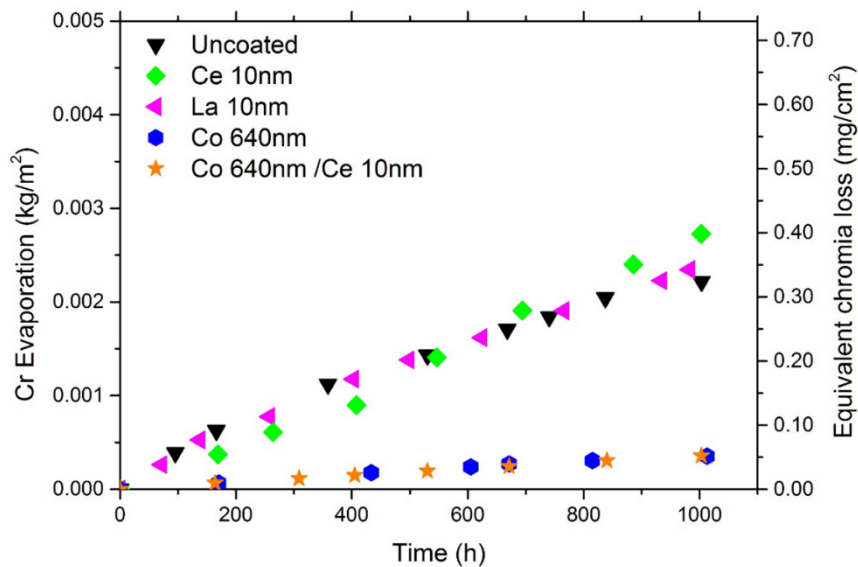


Figure 19 A comparison of time resolved Cr evaporation data for Sanergy HT coated with Ce,Co,Co/Ce and La and exposed at 850 °C in air+3% H₂O with a total flow of 6000 sml/min

Cr evaporation measurements reveal that the Ce coated steel experiences slightly higher volatilization rates than in the uncoated case. However, when the steel is coated with 10nm of La, the evaporation rate is identical to that of the uncoated steel. This could be due to the redox properties of the Ce rich particles on or close to the surface, a property not possessed by La; the particles are visible after both shorter and longer exposure times. Alternatively, the higher evaporation rate could also be related to the

finer grain structure of the outer spinel on the Ce coated sample compared to for the uncoated steel (Paper IV).

7.3. Oxide Scale Development on Coated and Uncoated Sanergy HT in air+3% H₂O at 850°C up to 1000 h

7.3.1. The uncoated steel

The oxide scale formed on the uncoated up to an exposure time of 1000 h is well adherent and dual layered, consisting primarily of an inner chromia (Cr₂O₃) and outer spinel (Cr,Mn)₃O₄ layer. The very initial stages of oxidation, however, produce no apparent ordering within the scale. This is visible in Figure 20 which shows quantitative TEM-EDX elemental maps of the uncoated steel after 1h of exposure. The oxide consists of an outer front rich in Cr, Mn and Fe. A Mn rich zone is identified beneath the mixed, outer oxide.

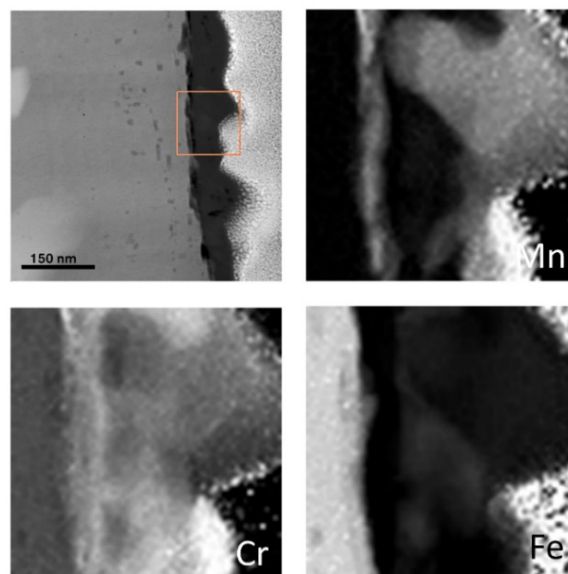


Figure 20 Quantitative TEM-EDX maps of the uncoated steel after 1h of exposure at 850°C in air+3% H₂O and a total flow rate of 6000 sml/min (43)

After 168h (Figure 21), the steel shows a well ordered oxide with a ~1 µm outer spinel and slightly thicker inner chromia layer. Laves phase precipitates are detected primarily along the alloy grain boundaries. These particles are known to improve oxide adhesion in this context by trapping some of the Si present in the alloy matrix and minimising

SiO₂ scale formation at the metal-oxide interface (4, 25). Internal oxide precipitates consisting of Ti-oxide are visible below the metal-oxide interface. In addition to this, Mn is detected in some regions along the metal oxide interface. Thermodynamics predicts the stability of the cubic Cr-Mn spinel at this interface (44, 45) and this is established using TEM diffraction. TEM-EDX quantitative maps have shown that this phase is present in some but not all regions along the said interface. While the presence of the cubic Cr-Mn spinel is expected from thermodynamics, its absence in some cases is attributed to the electrochemical nature of the oxidation process that drives the Mn outwards towards the scale-gas interface (Paper III).

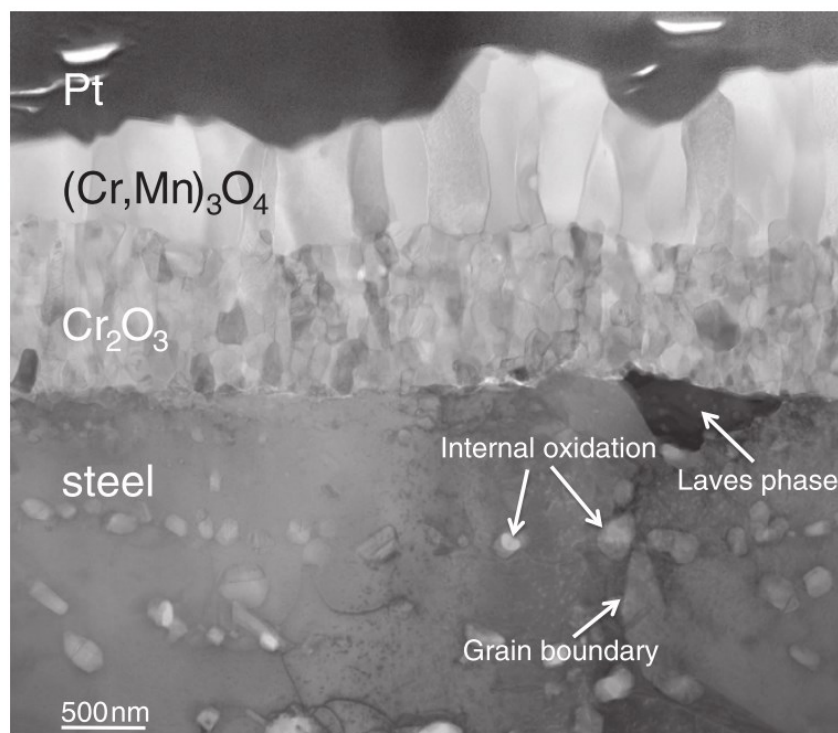
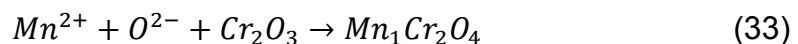


Figure 21 TEM Bright Field (BF) image of the uncoated steel after 168h of exposure at 850°C in air+3% H₂O and a total flow rate of 6000 sml/min

The outward diffusing Mn²⁺ reacts with the chromia at the chromia-spinel interface forming new Cr-Mn spinel according to Equation 33:



It is thus suggested that the formation of the Cr-Mn spinel occurs due to reaction of the migrating Mn²⁺ ions with the chromia layer (Paper III).

The steel after 1000h has a 6-7µm thick scale while the outer spinel is 1.5-2 µm thick (Figure 22) while the chromia layer is 5-6 µm thick. The presence of Fe in the outer

spinel can be attributed to the outward diffusion of Fe during the very initial stages of oxidation (see Fe map in Figure 20). No Mn is detected in the alloy implying that it has been consumed in spinel formation.

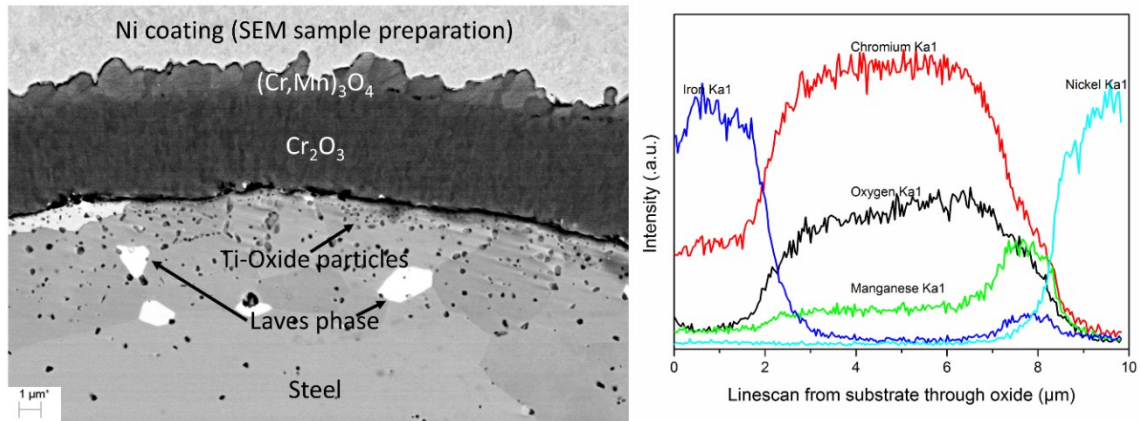


Figure 22 Left: SEM-BSE image of the uncoated steel after 1000h of exposure at 850°C in air+3% H₂O and a total flow rate of 6000 sml/min. Right: SEM-EDX linescan from the bulk through the oxide of the uncoated steel after 1000h of exposure at 850°C in air+3% H₂O and a total flow rate of 6000 sml/min

7.3.2. Ce 10nm Coating

The initial stages of the oxidation process provide indications of the reasons behind a retarded oxidation rate when the steel is coated with Ce. After 1h, the oxide is well ordered with an outer layer consisting of Cr and Mn and an inner Cr rich zone (Figure 23 (46)). A Ce enrichment is visible as bright spots along the interface between the two layers. This structure is in contrast to the uncoated case (Figure 20) where the oxide formed after 1 h exhibits a lesser degree of ordering. The Ce coating is thus believed to promote the formation of a protective oxide.

After 168h, an internal oxidation zone of Ti-oxide particles is visible as in the uncoated case. The chromia layer is about 500nm thick while the spinel is around 1 μm thick. The total scale thickness is thus less than for the uncoated steel after the same duration of exposure. Ce rich particles are identified within the spinel close to the scale-gas interface and on the oxide surface (Paper III).

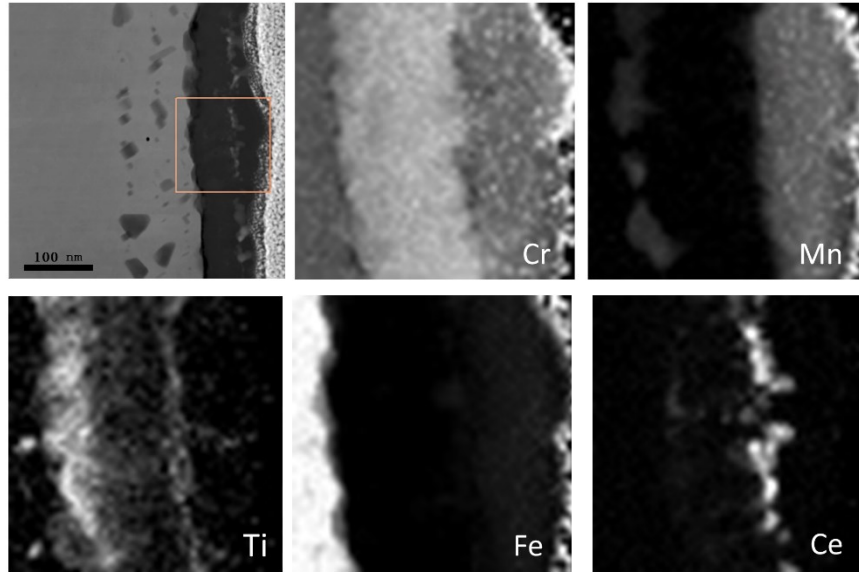


Figure 23 Quantitative TEM-EDX maps of Ce 10nm coated Sanergy HT after 1h of exposure at 850°C in air+3% H₂O with a total flow rate of 6000 sml/min (46)

7.3.3. Co 640nm Coating

During the early stages of oxidation, significant interdiffusion occurs between the steel and the coating. After 1 h, an outer double layered spinel forms over an inward growing chromia layer (Figure 24). EDX analysis reveals that the double layered (Co,Mn,Fe)₃O₄ spinel has an inner Fe rich region with an Fe:Co ratio of 9:1. The outer spinel has a Fe:Co ratio of 1:1 (43). In addition to this, Cr-Mn particles are detected, concentrated primarily along the metal-oxide interface. Thermodynamics suggests that this is likely to be a Cr-Mn spinel, the same as for the uncoated steel. Mn diffuses outwards, from the Mn rich region just below the metal-oxide interface, along grain boundaries. The Co spinel is therefore enriched in Mn with time.

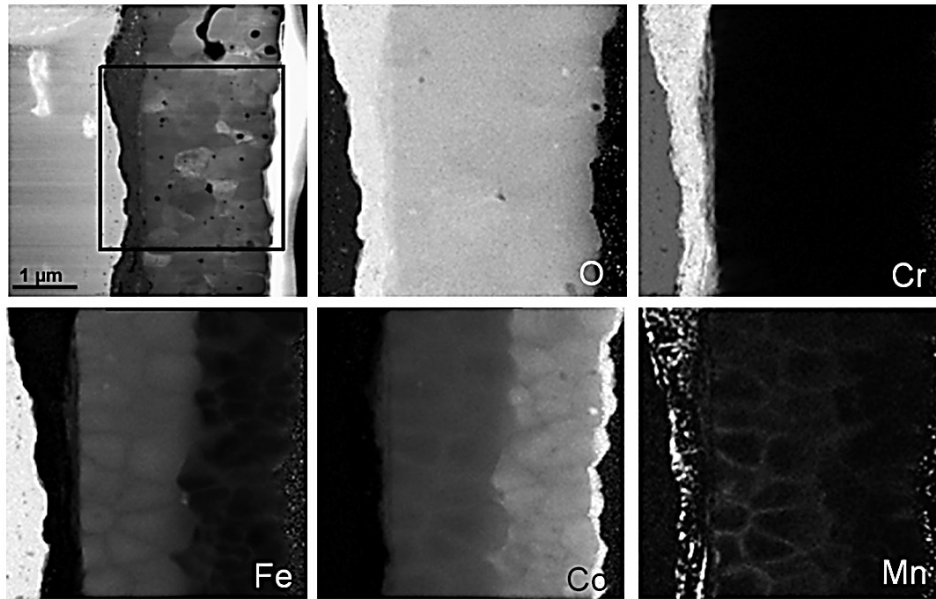


Figure 24 Quantitative TEM-EDX maps of Co 640nm coated Sanergy HT after 1h of exposure at 850°C in air+3% H₂O with a total flow rate of 6000sml/min (43)

After 168h (Figure 25), the total scale thickness is ~4 μm. The inner chromia layer is almost pure while the outer oxide is a spinel made up of Co,Fe and Mn with very little Cr.

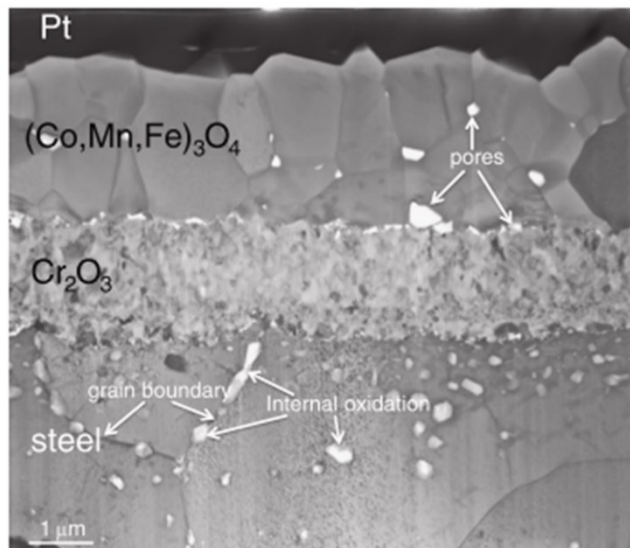


Figure 25 TEM-BF image of Co 640nm coated Sanergy HT after 168h of exposure at 850°C in air+3% H₂O at a total flow rate of 6000 sml/min

The composition varies between $\text{Co}_{1.4}\text{Fe}_{1.0}\text{Mn}_{0.6}\text{O}_4$ near the chromia spinel interface and $\text{Co}_{2.3}\text{Fe}_{0.4}\text{Mn}_{0.3}\text{O}_4$ near the scale-gas interface. The spinel thickness is around 2.5 μm and the CrMn zone under the chromia layer is still visible. The significantly lower evaporation rates measured from the Co coated material can be attributed to the

formation of a Co-Mn Spinel (Paper III). The thickness of the Co coating affects its ability to inhibit Cr evaporation. However, it is observed that the gains from increasing the Co coating thickness beyond around 640 nm is unlikely to further reduce the Cr evaporation rate to a significant extent. (Figure 26).

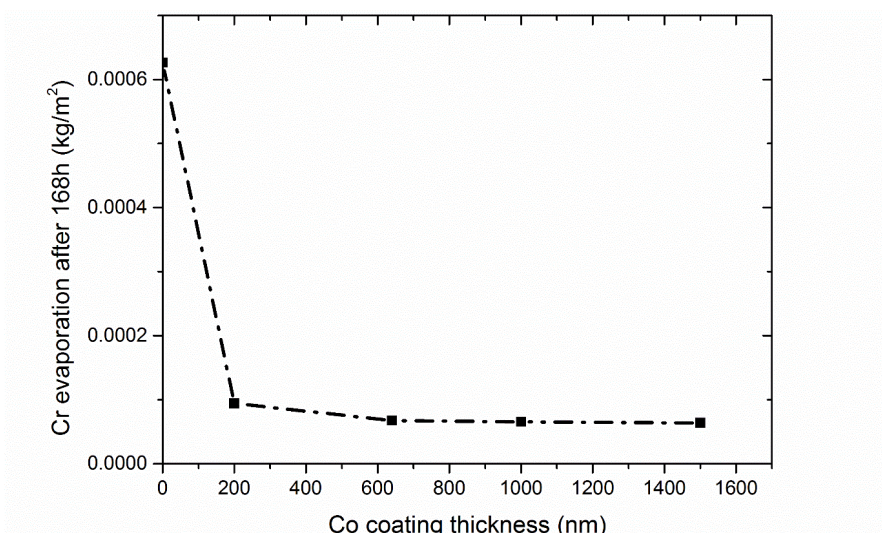


Figure 26 The thickness dependence of Co coatings on Cr evaporation. The exposures were carried out isothermally over 168h at 850°C in air+3% H₂O at a total flow rate of 6000 sml/min.

7.3.4. Co 640nm / Ce 10nm Coating

After 1 h of oxidation, the Ce coating clearly demarcates what is expected to be the initial interface between the Co coating and the steel (Figure 27).

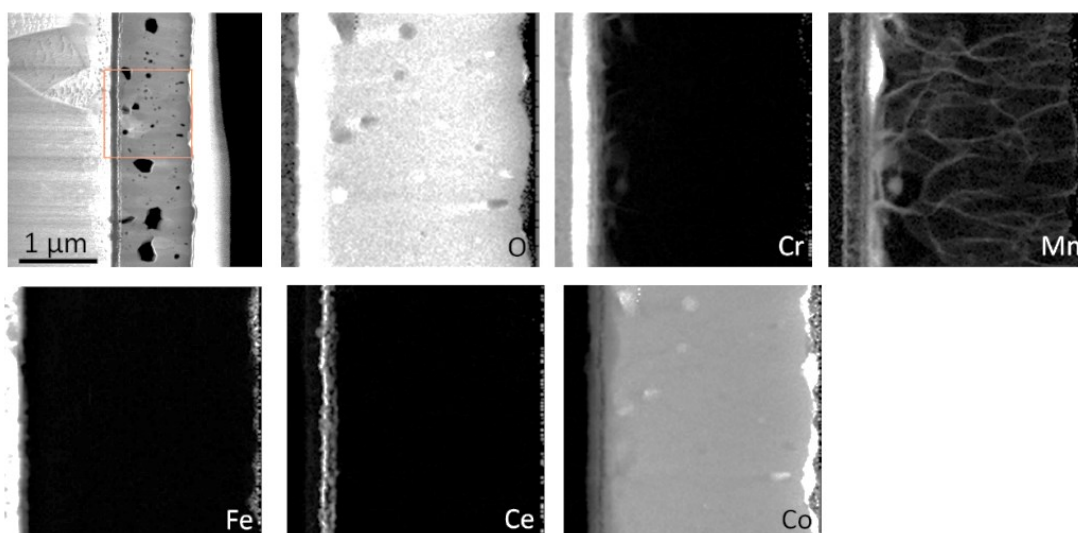


Figure 27 Quantitative TEM-EDX maps of Co 640nm/ Ce 10nm coated Sanergy HT after 1h of exposure at 850°C in air+3% H₂O with a total flow rate of 6000sml/min

As in the case where only a Ce coating is present, the interdiffusion between the Fe in the steel and the coating is prevented by the Ce rich layer. However, Mn diffuses outwards through the oxide grain boundaries as in the case of the purely Co coated steel.

After 168h, the oxide is dual layered with a total thickness of approximately 2.5 μm . The spinel layer is about 1.5 μm thick and incorporates a Ce rich band about 0.6 μm above the chromia layer (Figure 28). The Ce rich particles contain between 13-20 at% Ce. The composition of the spinel below the Ce band just above the chromia layer is $\text{Co}_{1.9}\text{Cr}_{0.7}\text{Mn}_{0.4}\text{O}_4$ and $\text{Co}_{2.5}\text{Cr}_{0.1}\text{Mn}_{0.4}\text{O}_4$ at the scale-gas interface. This drop in Cr concentration after the Ce rich particles could be attributed to the retardation of outward migration of Cr ions through the scale by Ce (Paper III).

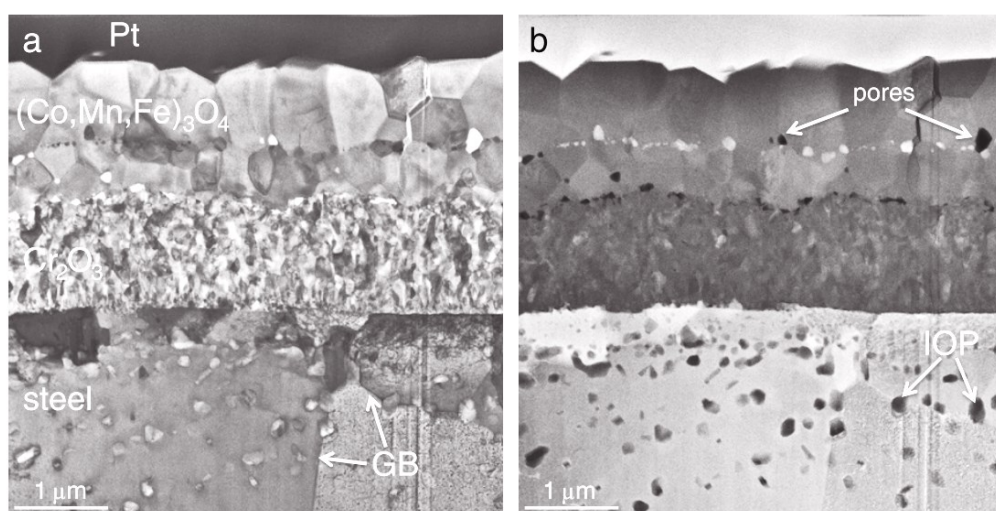


Figure 28 (a) Bright field STEM and (b) HAADF STEM micrographs of the oxide scale grown on the Ce/Co-coated sample at 850°C for 168 h. GB = grain boundary. IOP = internal oxidation particles

7.4. The Oxidation and Cr evaporation Properties of Coated and Uncoated Sanergy HT beyond 1000 h

The gravimetrically measured mass gain shows significant spread for exposure durations that last longer than 1000 h. In general, the effect of the Ce coating on oxidation is reflected in the lower mass gains for the Ce and Co/Ce coated samples compared to the uncoated and Co coated samples respectively. However, the erratic mass gains after longer exposure intervals (<1500 h) are not reflective of the protective oxide morphologies identified by microanalysis. The Reasons behind this spread in

data and a re-evaluation of the kinetics based on experimental evidence will be presented in Section 8. A brief discussion of the oxide microstructures after 3000 h are presented in Section 7.5. The evaporation rate measured for all materials after 3000 h is found to be relatively unchanged compared to that after 1000 h. It is thus assumed that the evaporation rate remains relatively constant after the initial period of stabilisation.

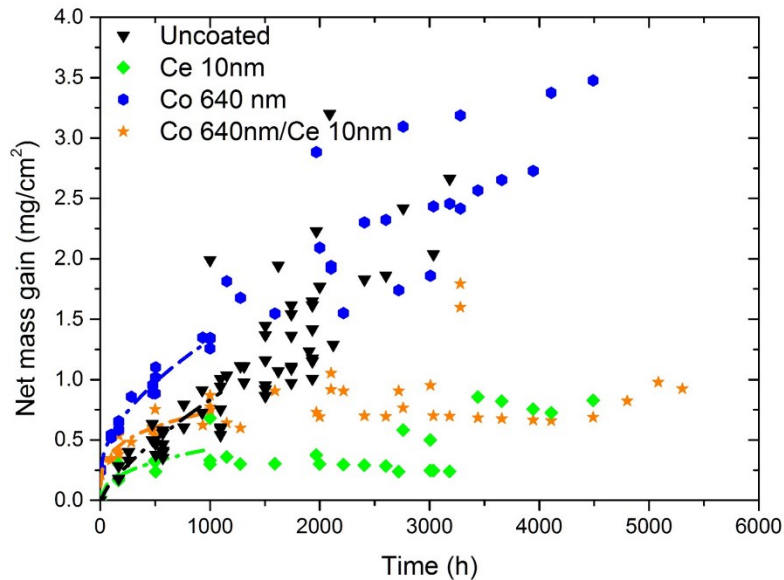


Figure 29 A comparison of net mass gain data for Sanergy HT coated with Ce, Co and Co/Ce exposed at 850 °C in air+3% H₂O with a total flow of 6000 sml/min

7.5. Oxide Scale Development on Coated and Uncoated Sanergy HT in air+3% H₂O at 850°C beyond 1000 h

7.5.1. The uncoated steel

The oxide on the uncoated steel is around 13 μm thick. The chromia phase is measured to be 11-12 μm while the spinel is 1-2 μm thick. Pores are visible along the metal-oxide interface and in the chromia scale. The nominal Fe concentration in the spinel is around 1-2 at%.

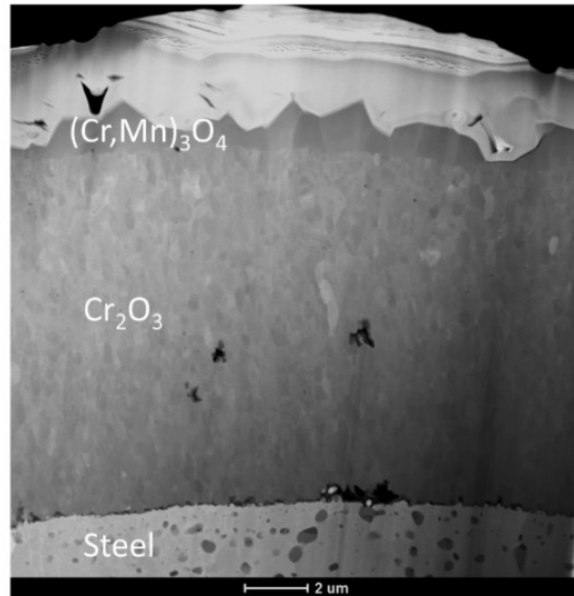


Figure 30 TEM-HAADF image of the uncoated steel after 3000h of exposure at 850°C in air+3% H₂O and a total flow rate of 6000 sml/min

7.5.2. Ce 10nm Coating

After 3000h, the total scale thickness is 5-6 μm with a chromia thickness of around 4 μm as opposed to 11-12 μm in the uncoated case. A reduction in pore concentration at the metal-oxide interface for the Ce coated steel compared to the uncoated steel is apparent if the cross sections after 3000h are compared. The nominal Fe concentration in the spinel for the uncoated case is around 1-2 at% while for the Ce coated steel, it is about 0.5 at% (46).

EELS (Electron Energy Loss Spectroscopy) analysis on the grain boundaries of the thermally grown oxide on Ce coated Sanergy HT after 3000 h of oxidation suggest that Ce decorates the grain boundaries of the spinel layer but is absent in the chromia grain boundaries. The absence of Ce along the chromia grain boundaries suggests that the improved oxidation resistance in this case might not be the result of a retardation of Cr³⁺ outward transport but a consequence of inhibited O²⁻ transport along the spinel grain boundaries (Paper IV). In contrast, most investigations attribute improved oxidation resistance of the steel to the segregation of reactive elements to the chromia grain boundaries e.g. (38, 39, 42). The reason for this discrepancy is unknown but might be related to the scale loss due to evaporation. While evaporation occurs at the spinel-gas interface, the result is a net consumption of the chromia layer (around 6μm per side based on evaporation measurements) due to its conversion into spinel (see

Section 7.3.1) This might result in a migration of the Ce particles in a manner that has not been observed in other studies.

7.5.3. Co 640nm Coating

The thickness of the oxide on the Co coated steel after 3000 h is 10-13 μm with a chromia thickness of 8-10 μm and a spinel thickness of 1.5-3 μm . The spinel phase consists of Co, Mn and Fe spinel where the nominal Fe concentration is 8 at% (43).

7.5.4. Co 640nm / Ce 10nm Coating

The Co/Ce coated steel has a well adherent scale after 3000h of oxidation. The total oxide is \sim 5-6 μm with a chromia thickness of \sim 3-4 μm . The voids visible at the metal-oxide interface for the Co coated sample are nearly absent in the Co/Ce case. The spinel on the Co/Ce coated steel contains virtually no Fe, indicating that Ce prevents the diffusion of Fe from the steel into the coating during the initial stages of the oxidation process. Ce rich particles are identified approximately 1 μm below the chromia-spinel interface.

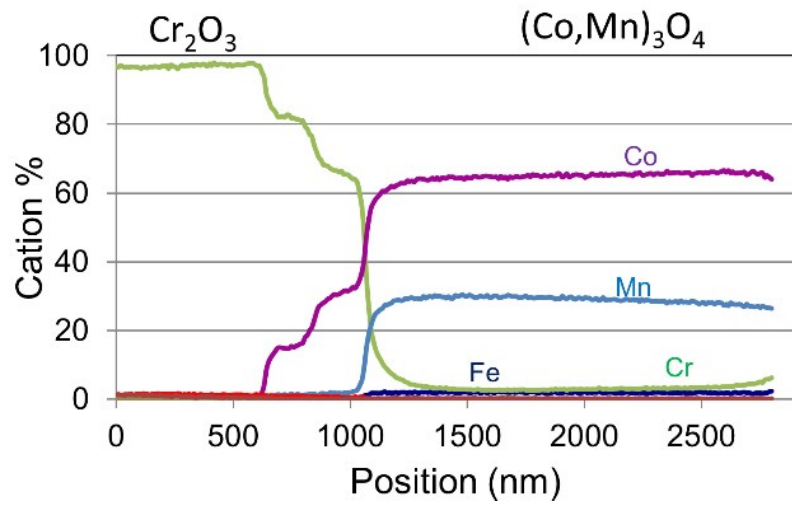
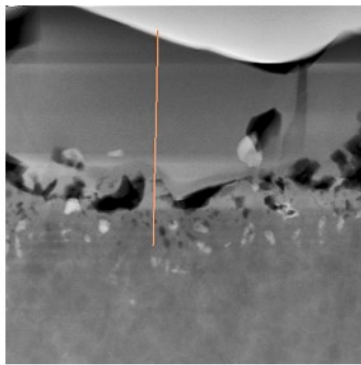
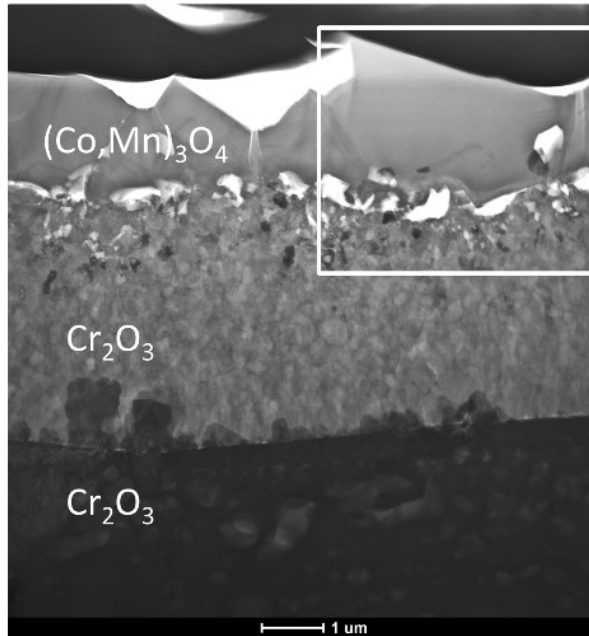


Figure 31 Top: TEM-BF image of the Co/Ce coated steel after 3000 h of exposure at 850°C in air+3% H₂O and a total flow rate of 6000 sml/min. The white box marks the region corresponding to the TEM-HAADF image at bottom left. The line marks the position of the quantitative EDX linescan through the oxide, shown bottom right

8. Estimation of the chemical lifetime of the coated and uncoated interconnect in cathode side environments

8.1. Quantifying the Impact of Coatings on Cr depletion

The oxide thickness is usually estimated from the gravimetrically recorded mass gain.

$$X_{\text{oxide}} = \gamma * \Delta m(t) / \rho_{\text{oxide}} \quad (34)$$

where $\Delta m(t)$ represents the mass gain at time t in mgcm^{-2} , γ is a stoichiometric factor converting oxygen pickup to equivalent oxide mass and is calculated to be 3.167 for Cr_2O_3 . X_{oxide} is the average oxide thickness and ρ_{oxide} is the average oxide density. The oxidation process manifests as scale growth; thicker scales thus imply a greater consumption of metal from the steel bulk. However, the measured mass gain $\Delta m(t)$ correlates to only a part of the total oxygen uptake experienced by the steel. Since part of the oxide formed volatilises, the true magnitude of oxygen uptake can only be calculated if the evaporation rate is known. If this quantity is referred to as the gross mass gain and the gravimetrically determined component as the 'net' mass gain then the prevailing mass balance can be described as in Equation 35:

$$\Delta m(t) = \Delta m_{\text{net}}(t) = \Delta m_{\text{gross}}(t) - \Delta m_{\text{evap}}(t) \quad (35)$$

Since the evaporation and gravimetric components are determined experimentally, it is more useful to write Equation 35 as:

$$\Delta m_{\text{gross}}(t) = \Delta m_{\text{net}}(t) + \Delta m_{\text{evap}}(t) \quad (36)$$

The evaporative component in Equation 36, $\Delta m_{\text{evap}}(t)$ is estimated from Equation 37:

$$\Delta m_{\text{evap}}(t) = \gamma / (\gamma - 1) \times \sum E^{\text{Cr}_i} \times \Delta t_i \quad (37)$$

The stoichiometric factor for converting Cr loss via evaporation to equivalent Cr_2O_3 loss is equal to 1.461 or $\gamma / (\gamma - 1)$, if written in terms of γ . E^{Cr_i} is the average evaporation rate of Cr over the i th measurement interval in $\text{mgcm}^{-2}\text{h}^{-1}$ and Δt_i is the duration in h over which E^{Cr_i} is applicable. It follows that by closing the mass balance, it also becomes possible to explicitly estimate the Cr content in the steel, as illustrated by Equation 38:

$$m_{Cr}(t) = m_{Cr,0} - (m_{Cr,oxide}(t) + m_{Cr,evap}(t)) \quad (38)$$

where $m_{Cr}(t)$ is the mass of Cr remaining in the steel, $m_{Cr,0}$ represents the mass of Cr originally available in the steel bulk, $m_{Cr,oxide}(t)$ represents the mass of Cr in the oxide and $m_{Cr,evap}(t)$ represents the evaporative component of Cr consumption.

But

$$m_{Cr,oxide}(t) + m_{Cr,evap}(t) = (\gamma - 1) \times \Delta m_{gross}(t) \quad (39)$$

In (37):

$$m_{Cr}(t) = m_{Cr,0} - (\gamma - 1) \times \Delta m_{gross}(t) \quad (40)$$

The stoichiometric conversion factor for converting gross oxygen uptake to its Cr equivalent is equal to 2.167, or $(\gamma - 1)$ if written in terms of γ . It follows that when no evaporation occurs, the gross mass gain is equal to the gravimetrically determined mass gain and Equation 36 can be adjusted accordingly. The quantity of Cr remaining in the steel, specified here in wt%, can then be estimated:

$$Cr_{rem}(t) = [(m_{Cr}(t)) / (m_{Cr}(t) + (\sum m_i - m_{Cr,0}))] \times 100 \quad (41)$$

where the term $\sum m_i$ in Equation 41 represents the sum of mass contributions of the individual alloying elements in the steel.

For exposure times longer than 1000 h, the uncoated steel subject to an evaporation reaction at the oxide surface exhibits atypical oxidation kinetics ('flow' mass gain in Figure 32). However, when the evaporation reaction is suppressed (see Section 5.1.1), the kinetics are in accordance with the parabolic rate law ('no flow' mass gain' in Figure 32). This is attributed to the breakaway oxidation of the sample edge (Figure 33) and results from the higher rate of metal consumption required to sustain a protective oxide scale at geometries with higher surface to volume ratios such as edges and corners (47, 48).

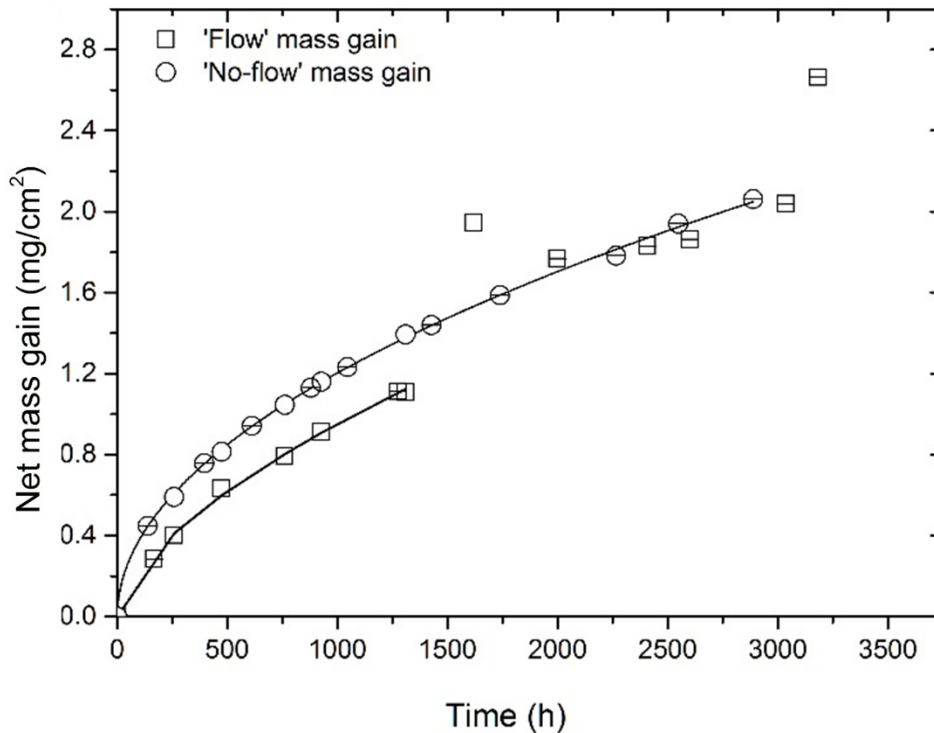


Figure 32 Mass gain data from representative samples under 'flow' (squares) and 'no-flow' (circles) conditions. The empty and marked symbols represent samples that have been exposed up to 1600 h and 3100 h respectively

While the enhanced metal consumption rate results in a Cr depletion zone towards the edge of the sample in both the 'flow' and 'no-flow' cases [29], it is the extraneous metal consumption resulting from Cr evaporation that eventually triggers the premature failure of the protective scale at the sample edge in the 'flow' case, as is evidenced by comparing the edges of samples exposed in the 'flow' (Figure 33 a-b) and 'no-flow' conditions (Figure 33 c-d).

The gravimetrically measured oxygen uptake or 'net' mass gain over longer exposure durations (>1000 h) can thus be deconstructed into two major components. The first contributor is the oxygen uptake due to growth of the protective chromia layer while the second is breakaway oxidation of the specimen edge. Since no breakaway edge oxidation is observed in the 'no-flow' condition, it is assumed that the 'net' mass gain in this case is composed entirely of the oxygen uptake due to growth of the protective oxide. However, in the flow condition, deviations from expected growth after ≈ 1200 h indicate that the 'net' mass gain measured after this time period consists of both components. This deconstruction is presented graphically in Figure 34 where the 'flow' mass gain is separated into its protective and non-protective components.

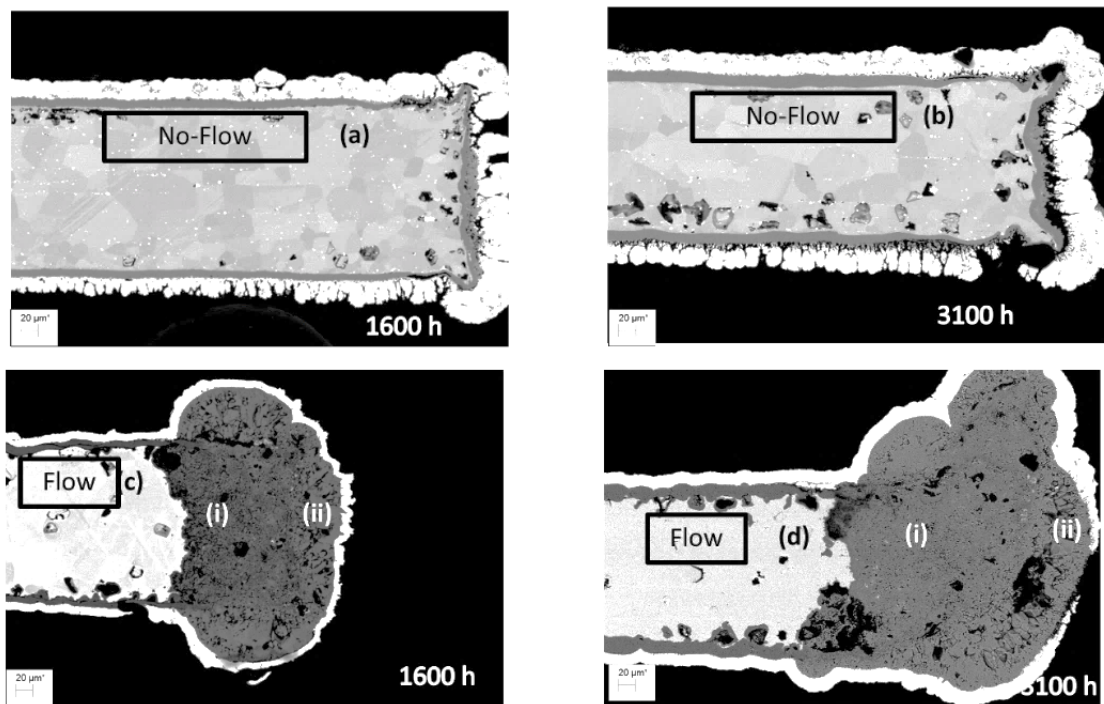


Figure 33 SEM-BSE Cross section along specimen edge of samples exposed in the 'no-flow' (a and b) and 'flow' (c and d) condition after 1600 h and 3100 h showing (i) Inward growing Fe-Cr oxide and (ii) outward growing Fe oxide. The samples have been electroplated with nickel after exposure, during SEM sample preparation

The validity of the deconvolution of the net 'flow' mass gain into its edge and surface components can be independently verified by using the edge corrected gravimetric data (curve E-F in Figure 34) and Cr evaporation data to estimate the extent of Cr depletion in the steel below the oxide scale away from the sample edge (see Equation 41 in Section 8.1) (Paper II)

While the evaporation reaction occurs at the scale-gas interface, the Cr volatilized away is assumed to be readily replaced in the spinel by consumption of some of the chromia as previously discussed. A flat Cr profile through the bulk is observed from SEM-EDX linescans performed on uncoated Sanergy HT after 3000h of oxidation (Figure 35). This implies that the delivery of Cr to the metal-oxide interface is fast enough to replace any Cr leaving the interface and diffusing outwards through the oxide scale. This observation is consistent with previous work on modeling Cr consumption in ferritic interconnects between 800-900°C (49)

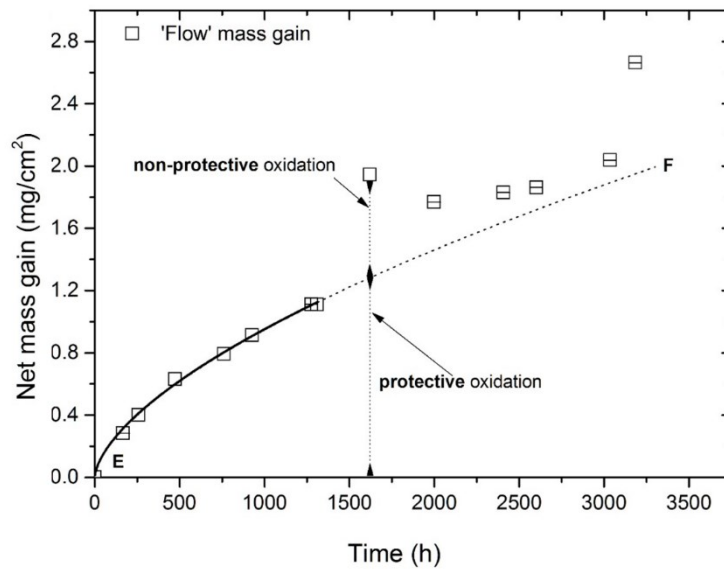


Figure 34 Gravimetric data ('net' mass gain) in the 'flow' condition de-convoluted to indicate the mass gain contributions from protective and non-protective oxide growth, achieved by extrapolating the experimental data collected up to 1200 h. The curve E-F thus represents the mass gain contribution from protective oxide growth on the surface of the steel while any extraneous mass gain contribution represents non-protective oxide growth on sample corners and edges

The calculation (see Section 8.1) reveals a very sound correlation between concentrations predicted based on the edge corrected oxidation data and EDX measurements away from the sample edges (Figure 36). Further, it is also noted that the effect of Cr evaporation is to limit the oxide thickness such that the long-term Cr depletion rate in the steel is higher over longer durations, relative to if the evaporation reaction had been suppressed (Paper II)

An indication of the time to chemical failure of a protective oxide due to depletion of the scale forming element (Cr) can be found by observing the rate of depletion of Cr in the steel bulk (Figure 36). After 3000h, the Cr content in the steel for the uncoated material is 15%, which is considered dangerously close to the empirically observed limit for breakaway corrosion of chromia formers around the chosen exposure temperature (50). When Cr evaporation is not considered, the calculated Cr content remaining is 18%. This overestimation is highlighted in Figure 36 where lifetime estimates from 'net' mass gain i.e. only gravimetric data corrected for edge oxidation and gross mass gain i.e. gravimetric and evaporation data, are compared. An extrapolation of the available oxidation data suggests that neglecting the effect of evaporation would result in an overestimation of the useful life of the uncoated steel by 12000 h, if a critical Cr content of 15 wt% is assumed.

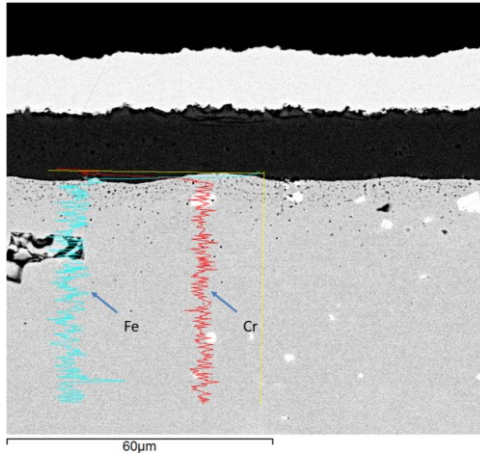


Figure 35 SEM-EDX linescan through the bulk of uncoated Sanergy HT showing a flat Cr profile after 3000h of exposure at 850°C in air+3% H₂O at a total flow rate of 6000 sml

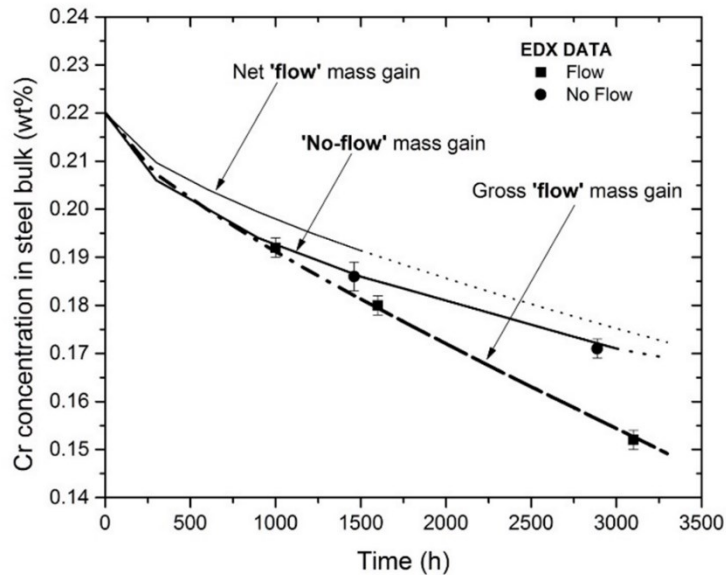


Figure 36 A plot of Cr concentration over time in the steel, calculated based on oxidation and Cr evaporation data (lines) and measured using quantitative EDX point analysis (circles and squares). The gravimetric information is based on the curve E-F in Figure 34

A similar analysis can be extended to the coated samples to verify if the spread in gravimetric data is a by-product of edge oxidation. 'By first measuring the Cr concentration in the steel after various exposure durations, it becomes possible to estimate the gross mass gain, or cumulative oxygen uptake associated with oxide growth and Cr evaporation independent of any edge effects (Figure 37, Paper V).

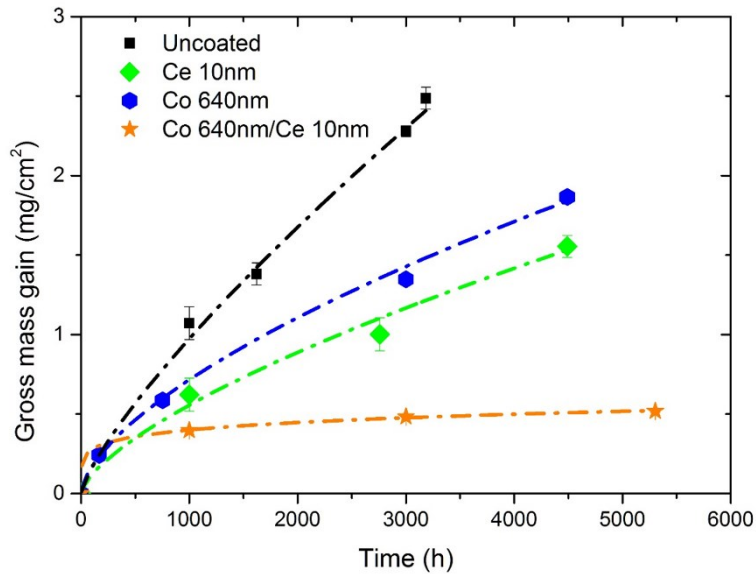


Figure 37 Expected gross mass gain for the uncoated and coated steel derived from EDX point analysis in the steel bulk after exposure at 850 °C in air+3% H₂O and a total flow rate of 6000 sml/min

It follows that the 'net' mass gain can be computed if the evaporation rate over the exposure duration is known (see Equation 35 in Section 8.1). Such a calculation, taking into account the mass gain contribution of the Co layer where required, suggests a trend for the evolution of the 'net' mass gain independent of edge effects (Figure 38). The dashed lines represent so-called para-linear kinetics and are characteristic of a diffusion controlled oxidation process subject to a volatilisation reaction at the oxide surface (see Section 3.2). This data can first be used to make qualitative inferences regarding the effect of coatings on the oxidation properties of the steel. Since the limiting thickness is defined by the kinetic competition between the oxidation reaction and the volatilisation reaction, it can be deduced that a lower limiting thickness would imply a slower oxidation process for the same volatilisation rate. It is apparent by comparing data for the uncoated and Ce coated steel and Co and Co/Ce coated steel respectively that a limiting thickness is reached earlier when the 10nm thick Ce coating is present, implying that Ce reduces the oxidation rate of the steel. Any extraneous mass gain above the respective dashed lines in Figure 38 is thus believed to result from oxidation of the uncoated edge of the sample.

Parabolic rate constants derived from analysis of the para-linear curves in figure 32 suggest that the rate of oxide thickening for the uncoated steel is independent of the volatilization reaction; the parabolic rate constant for the oxide on the uncoated steel when the evaporation reaction was suppressed ($4 \times 10^{-13} \text{ g}^2 \text{ cm}^{-4} \text{ s}^{-1}$) is similar to that

estimated for the steel subject to a flow-rate independent evaporation reaction at its oxide surface ($5 \times 10^{-13} \text{ g}^2\text{cm}^{-4}\text{s}^{-1}$). Further, it is noted that the effect of the Ce coating is to reduce the oxidation rate by approximately one order of magnitude ($4 \times 10^{-14} \text{ g}^2\text{cm}^{-4}\text{s}^{-1}$). It is also observed that the calculated parabolic rate constant for the Co coated steel ($3 \times 10^{-13} \text{ g}^2\text{cm}^{-4}\text{s}^{-1}$) is similar but slightly lower than that of the uncoated steel, implying that the Co coating has almost no effect on the rate of scale growth of the protective oxide. In contrast, the parabolic rate constant for the Co/Ce coating ($9.8 \times 10^{-15} \text{ g}^2\text{cm}^{-4}\text{s}^{-1}$) is significantly lower than for the uncoated steel and somewhat lower than for the Ce coated steel. This suggests that the Ce coating affects the mobility of ionic species not just in the chromia scale but also in the Co-Mn spinel (Paper V).

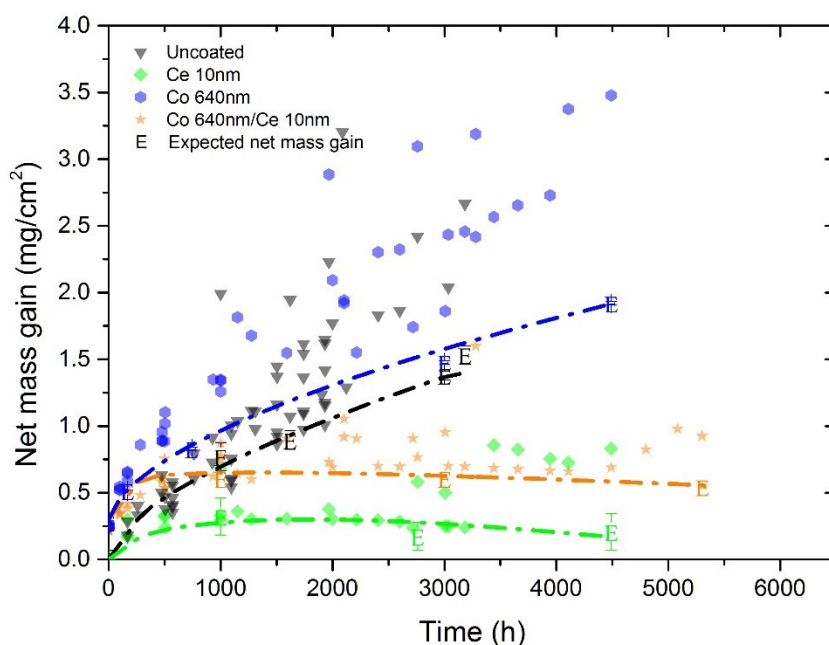


Figure 38 Net mass gain data for Sanergy HT coated with Ce, Co and Co/Ce exposed at 850 °C in air+3% H₂O with a total flow of 6000 sml/min. The dashed lines indicate the expected net mass gain based on EDX Cr depletion measurements in the steel, corrected for Cr evaporation and Co oxidation. The extraneous mass gain observed via gravimetry is attributed to oxidation of the sample edges

The effect of the Ce coating becomes especially apparent when oxidation data is represented in terms of Cr consumption as shown in Figure 39. The slightly higher metal loss due to evaporation notwithstanding, the Cr content of the steel after 3000h is around 19.5 wt% compared to around 15 wt% for the uncoated steel. This retardation in Cr consumption results in an increase of the estimated time to 15 wt% from 3000 to 9000 h.

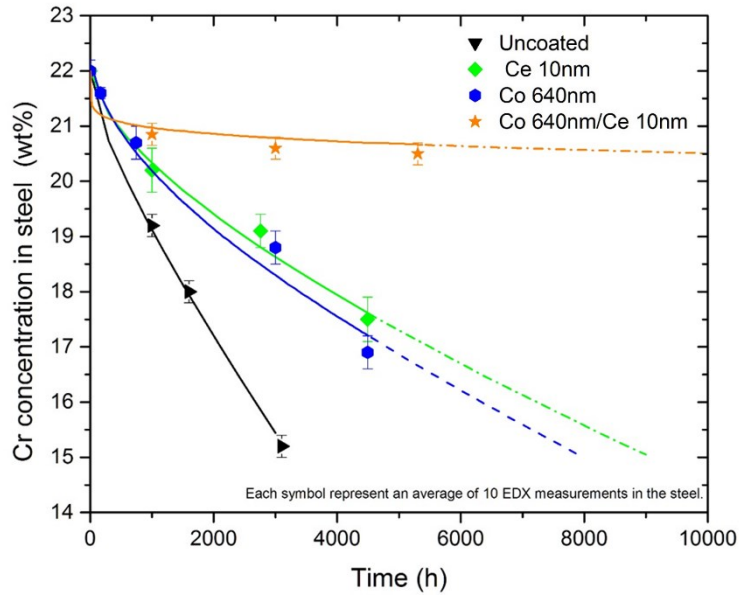


Figure 39 An estimate of Cr consumption over time calculated by combining gravimetric and Cr evaporation data for uncoated and coated Sanergy HT at 850°C in air+3% H₂O at a total flow rate of 6000 sml/min. The symbols represent the results of EDX point analysis in the steel while the dashed lines represent extrapolations based on the observed trend

The lower metal loss via the evaporation reaction experienced by the Co coated steel effectively extends the chemical lifetime of the steel by around the same extent as for the Ce coated steel. However, the combined Co/Ce coating dramatically improves the oxidation resistance properties of the steel: the Cr concentration in the Co 640nm/Ce 10nm coated steel is 20.5 ± 0.1 wt% even after 5300 h (Paper V).

9. Oxidation of Coated and Uncoated Interconnect materials in Ar-5% H₂+3% H₂O at 850°C

The fuel side environment of an SOFC has a relatively low oxygen partial pressure (of the order of 10^{-15} - 10^{-21} bar $p(\text{O}_2)$) at 850°C compared to 0.2 bar for the air side) and contains high amounts of water vapour. The oxidation rate of the uncoated steel in the low $p(\text{O}_2)$ environment is lower than in air ($7.72 \times 10^{-14} \text{ g}^2\text{cm}^{-4}\text{s}^{-1}$ compared to $4 \times 10^{-13} \text{ g}^2\text{cm}^{-4}\text{s}^{-1}$ in air from data in Paper II). Gravimetric data for uncoated and coated Sanergy HT exposed in Ar-5% H₂+3% H₂O (10^{-18} bar $p(\text{O}_2)$) at 850°C) suggest that while reactive elements appear to have a positive impact on the oxidation properties of the steel, the presence of Co has no net positive effect on oxidation performance (Figure 40, Paper VI).

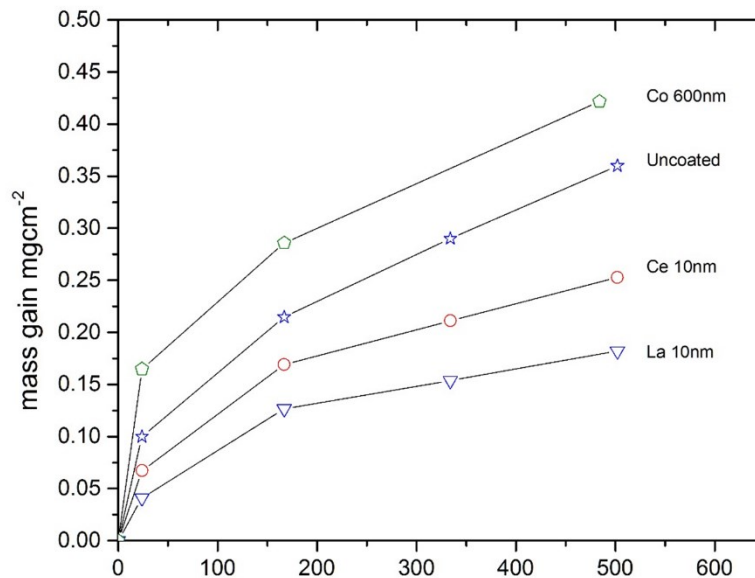


Figure 40 Mass gain of the coated and uncoated steel in Ar-5% H₂+3% H₂O at 850°C without any pre-oxidation step

The effect of the pre-oxidation treatment, or 'priming' step appears to be to retard the oxidation rate of the steel in the simulated fuel side environment (Figure 41). Niewolak et al. compared oxide scale growth rates on interconnect steels in air and H₂-H₂O at 800°C. They concluded that the oxidation rate of the steel in the H₂-H₂O environment is initially higher but drops below that in air once a gas-tight spinel layer has formed (51). The lower oxidation rate for the pre-oxidized samples can thus be qualitatively explained by the fact that oxidant access to the chromia layer during exposure in the simulated fuel side environment is significantly hindered by the outer spinel that forms

during the pre-oxidation step. In addition, the dense oxide that results from the pre-oxidation step presents a longer diffusion path for the ionic species participating in oxide formation. In a diffusion controlled oxidation process such as that observed in this study, the reaction rate reduces as a consequence.

It is observed that the oxide morphology of the uncoated steel is similar to that of on the air side, consisting of an outer Cr-Mn spinel over a dense chromia layer (compare Figure 43 to Figure 21). In contrast, the Co-Mn spinel is found to be unstable in the simulated fuel side environment. The oxide morphology on the Co coated steel after exposure in the fuel side environment consists of metallic Co dispersions in the protective oxide and Co nodules on the surface of the spinel with dark inclusions in the Co nodules (Figure 44, Paper VI). The higher mass gain for the Co coated steel in the simulated fuel side environment is postulated to be a result of the oxidation of metal ions from the steel that diffuse into the Co matrix at the very beginning of the oxidation process (see Figure 24). These metal oxides manifest themselves as dark spots in the metallic Co nodules on the surface of the oxide (Figure 44). Apart from reducing the oxidation rate of the steel, the 10nm thick La coating reacts with the thermally grown oxide to form a La-perovskite at the chromia spinel interface (Figure 45).

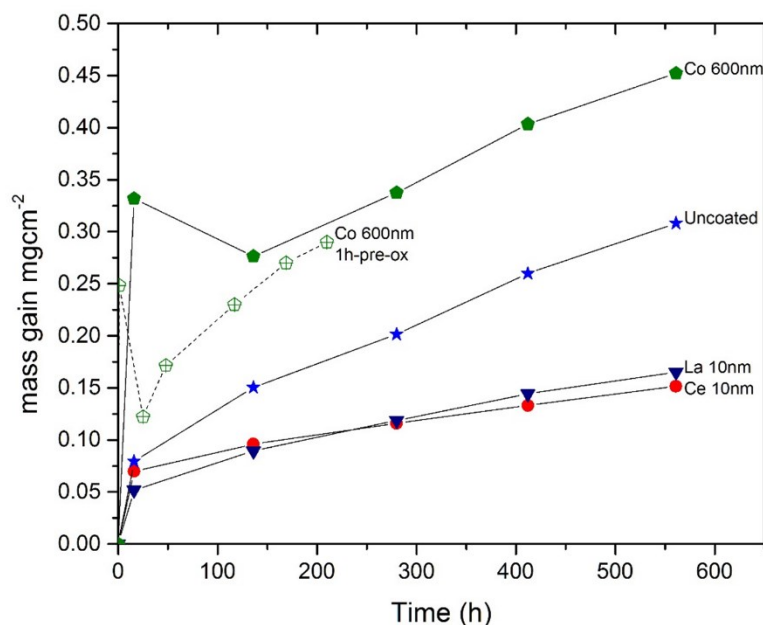


Figure 41 Mass gain of the coated and uncoated steel in Ar-5% H₂+3% H₂O at 850 °C after a 16 h pre-oxidation step in air

Literature suggests that the electronic conductivity of La-perovskites under low p(O₂) conditions (e.g. (52)) is generally higher than that of the Cr-Mn spinel (53) and the chromia layer (54). A sufficiently thick La coating could then result in an oxide

morphology consisting primarily of a La-perovskite over a thin, protective chromia layer which could improve the otherwise poor conductivity of the oxide layer in low $p(\text{O}_2)$ environments.

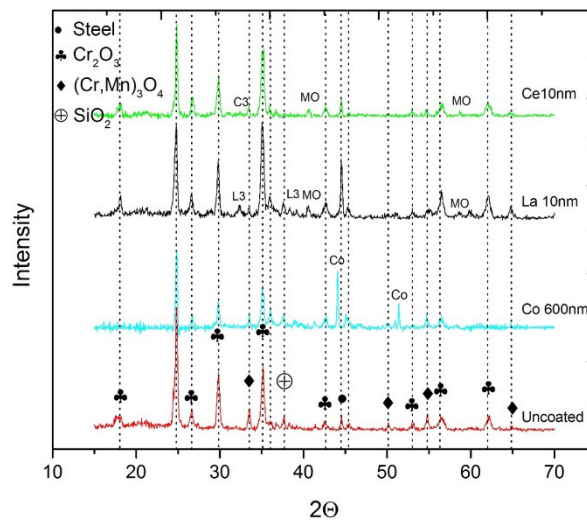


Figure 42 XRD diffractograms for the coated and uncoated steel after exposure in Ar-5% H_2 +3% H_2O at 850 °C. Common phases are marked with symbols. Additionally, phases specific to a sample are marked as: (MO)-Manganosite (MnO); (L3)- La Perovskite; (C3)-Ce perovskite (Co)- Metallic Co.

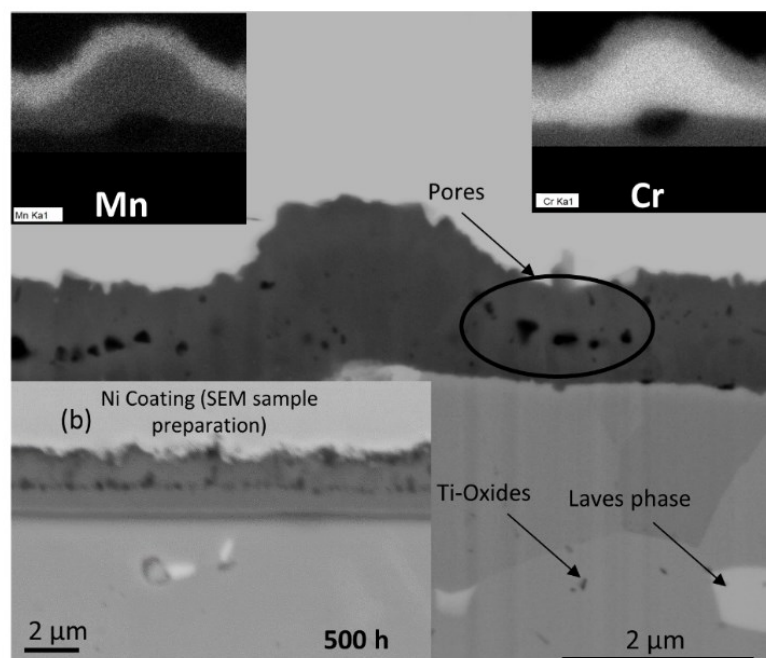


Figure 43 (a) SEM-BSE image of a Focused Ion Beam (FIB) prepared lift-out of uncoated Sanergy HT after 168 h of oxidation in Ar-5% H_2 +3% H_2O at 850 °C and inset (b) SEM-BSE image of the mechanically prepared cross section of uncoated Sanergy HT after exposure in Ar-5% H_2 -3% H_2O at 850 °C for 500 h. (a) contains EDX maps of the oxide showing a Mn rich outer region and a Cr rich inner region (top left and right respectively)

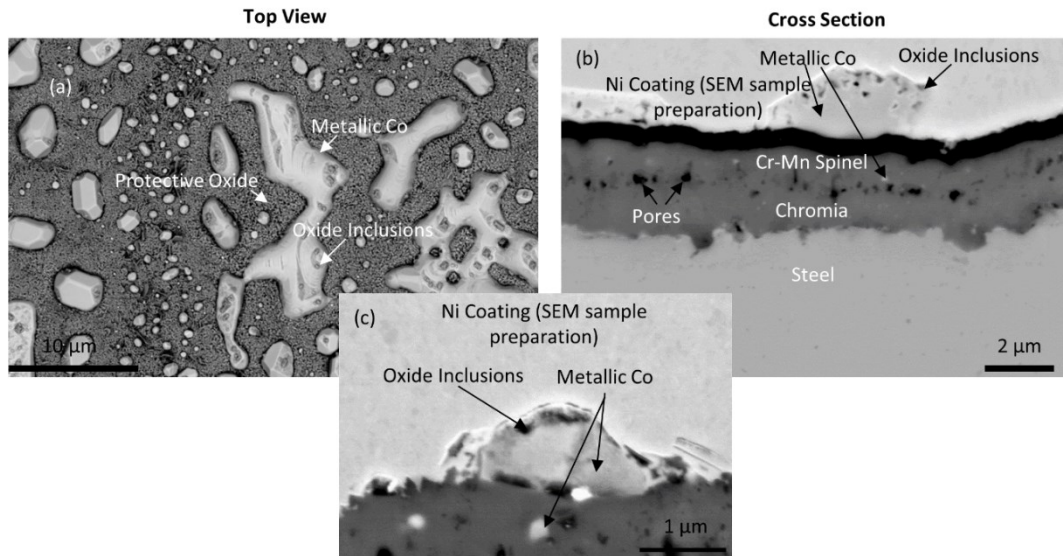


Figure 44 SEM-BSE images of the Co 600nm coated steel after exposure in Ar-5% H₂+3% H₂O at 850°C for 500 h showing (a) sample surface; (b) cross section of steel and oxide and (c) higher magnification image of metallic Co nodule with oxide inclusions

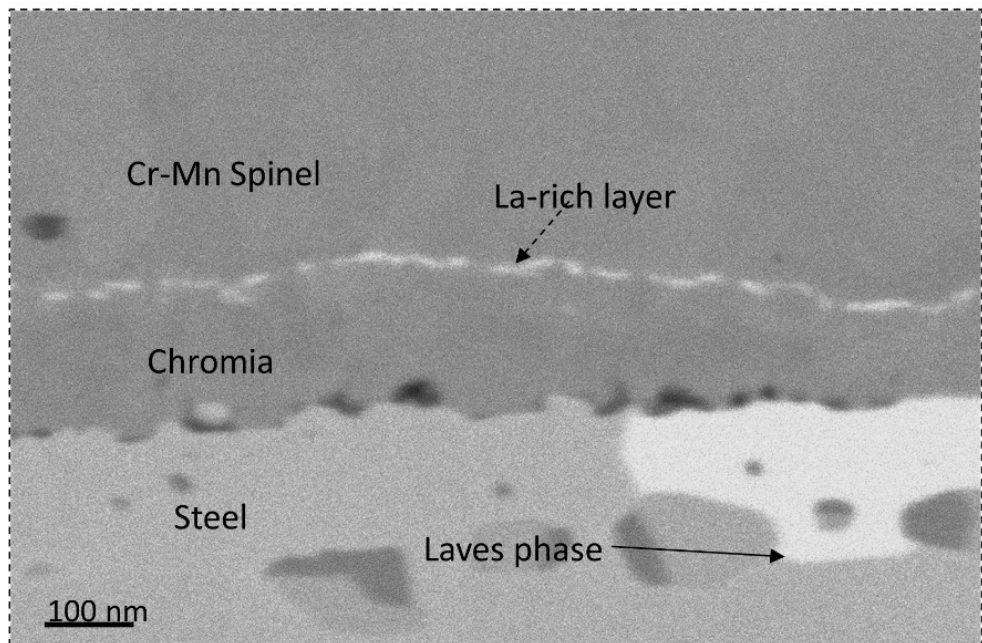
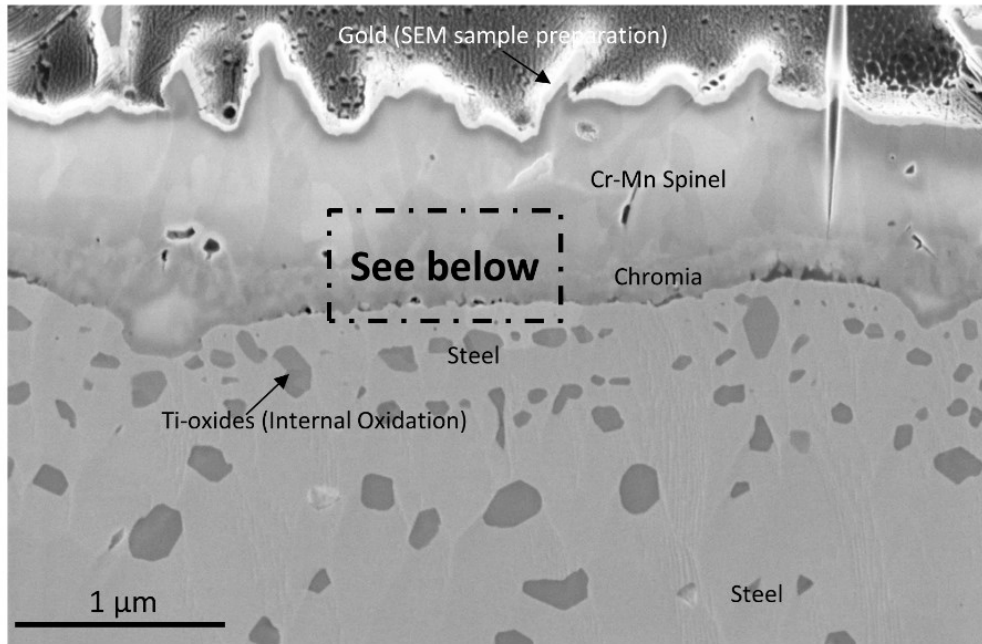


Figure 45 Broad Ion Beam (BIB) cross section of the La 10nm coated steel Ar-5% H₂+3% H₂O at 850 °C for 500 h. The image has been acquired with a secondary electron in-lens detector.

10. Conclusion

The long-term durability of the bipolar plate or interconnect plate that allows individual cells to be stacked is critical to the stable performance of the Solid Oxide Fuel Cell (SOFC) system, operating between 600-1000°C. The vastly differing conditions of the air and fuel side environments place unique requirements on either side of the bipolar plate. The oxidation performance of the ferritic steel developed for SOFC interconnect applications is improved by the addition of rare earth elements (e.g. La, Hf, Zr) to the alloy matrix. The steels also contain varying amounts of Mn to reduce the volatilisation rate of the thermally grown oxide in air side environments, by formation of a Cr-Mn spinel cap layer. However, it is established that the observed long term oxidation and Cr evaporation (scale volatilisation) rates far exceed that required to ensure stable performance of the SOFC.

The application of a 640nm thick layer of metallic Co results in the formation of a stable Co-Mn spinel cap layer, that is enriched with time in Mn by outward diffusion from the steel through the oxide grain boundaries. Time resolved Cr evaporation measurements over 1000 h show that the Co-Mn spinel produces an order of magnitude reduction in the Cr volatilisation rate relative to the uncoated steel. The reduction is attributed to the lower activity of Cr in the Co-Mn spinel relative to the Cr-Mn spinel formed on the uncoated steel.

The oxidation and Cr evaporation properties of the steel can be further improved by tailoring its surface properties using coatings. It is shown that a 10nm thick layer of Ce applied to the metal surface prior to oxidation brings about a significant reduction in the oxidation rate of the steel. The results suggest that this is brought about by influencing ionic transport through the oxide grain boundaries.

A duplex coating consisting of 10nm of Ce under 640nm of Co results in slower oxidation kinetics and lower Cr evaporation than for the uncoated steel. The interdiffusion between metal and coating is minimised in this case by the Ce coating, which acts as a diffusion barrier to the outward migration of Fe. Data combining long term measurements of oxidation and evaporation rate with Cr depletion measurements in the steel suggests that the Ce coating might influence ionic transport kinetics in not just the chromia layer but also the Co-Mn spinel.

Both oxidation and Cr evaporation are flow-rate dependent phenomena, making data collected in indeterminate flow environments, such as box furnaces, misrepresentative of the oxidation and Cr evaporation properties of the steel. By combining time resolved oxidation and Cr evaporation data, it is seen that the Cr consumption rate in high-flow environments is accelerated compared to in stagnant or low flow environments. This enhanced depletion of the protective scale forming element significantly reduces the time to chemical failure of the oxide scale.

In simulated fuel side environments, Co coatings do not form a thermodynamically stable duplex oxide like in cathode side environments. However, the oxidation rate is reduced by a factor 2-3 when nanoscale coatings of reactive elements are applied (Ce or La), resulting in a thinner chromia scale. A pre-oxidation step in air effectively reduces the oxidation rate of the steel under simulated fuel side conditions, which is probably related to the hastened formation of a gas tight spinel layer that inhibits oxidant access to the steel.

11. Outlook

SOFCs employing anode, electrolyte and metal supported architectures have begun to show stable performance over several thousands of hours of operation, at the stack and system level e.g. (55-59). Following this, there appears to be a paradigm shift in the nature of discourse surrounding SOFCs from reliable performance to up-scaling and lowering system cost. The importance of driving down stack and system cost is evident when considering the price of a market-ready SOFC CHP system today: e.g. 18 000 € for the Hexis Galileo 1000N CHP unit producing 1 kW of electricity (58) and 20 000 € in Japan for the 700 W_{el} ENE-FARM type S (60). However, the commercial viability of solid oxide based electrochemical energy conversion systems might eventually be decided by market niches that are, as yet, less price sensitive than current areas of focus. Promising areas include, but are not limited to, grid-independent power for server farms, aircraft APUs (61) and electrolysis cells to produce synthesis gas.

The material cost of interconnects can be further reduced by shifting from speciality to lower cost steel-coating systems; the approximate price for a speciality steel such as Crofer 22H or Sanergy HT is around 10 times that of the steel AISI 441 at current volumes. Additionally, developing the interconnect around a commercial steel like AISI 441 that can be sourced from several manufacturers minimises the risk of getting locked-in to a material whose future availability is uncertain. While the Co/Ce coating has been shown to effectively limit oxidation and Cr evaporation rates independent of steel substrate (62) and decrease the air side ASR (63, 64), much work remains before the mechanisms behind the observed effects are fully understood.

It has been established that the nm scale Ce coating helps to effectively retard the oxidation of the steel in air side conditions. The mechanism by which this is achieved is, however, still a matter of debate. Further, the suitability of other reactive elements, such as La has not as yet been investigated in as much detail. The effects of reactive elements on the mechanical stability of the oxide under cycling conditions are also an area that requires exploration.

Further, when the interconnect is subject to dual atmospheres, the oxidation behaviour is markedly different, exhibiting breakaway corrosion well in advance of under single atmosphere conditions (65). The mechanisms behind dual atmosphere corrosion and

its prevention are of interest for the long term stability of SOFC systems. Additionally, the effect of high water vapour concentrations under low $p(\text{O}_2)$ conditions as encountered under high fuel utilisation are deleterious to the oxidation properties of the steel and needs further investigation. Like on the cathode side, coating strategies need to be explored to improve oxidation resistance and reduce the scale ASR in fuel side environments. Interactions with contact layers and electrodes in addition to the effect of current are also parameters worth considering in future studies.

12. Acknowledgements

My journey as a PhD student would have been impossible without the faith and encouragement of my supervisor Professor Jan-Erik Svensson and co-supervisor Assistant Professor Jan Froitzheim.

I could not have asked for a better group of fellow graduate students than Jan Grolig, Hannes Falk Windisch and Patrik Alnegren whose infectious enthusiasm kept me going. Thank you to Dr Christine Geers for the insightful discussions. Thank you to Sandra Gustafsson for all the administrative help.

A special thanks to Dr Sead Canovic for his guidance during the first year of my graduate studies and help with the SEM.

Thank you to Professor Lars Gunnar Johansson and Professor Itai Panas for sharing their knowledge of chemistry among other things.

Thank you to everyone at the division of environmental inorganic chemistry for the coffee room banter.

I would like to express my gratitude to Dr Jörgen Westlinder and Dr Mats W Lundberg at AB Sandvik Materials Technology for the fruitful cooperation over the years.

The High Temperature Corrosion Centre (HTC) along with the NaCoSOFC and METSAPP projects are acknowledged for their financial support.

Thank you to my parents, siblings, family and friends for their unconditional support.

And thank you to the city of Gothenburg and all the wonderful people I have met during my time here for helping me make this my home by the sea.

13. References

1. J. T. S. Irvine, *Solid Oxide Fuels Cells: Facts and Figures*, Springer, London (2013).
2. N. P. Brandon, S. Skinner and B. C. H. Steele, *Annual Review of Materials Research*, **33**, 183-213 (2003).
3. W. J. Quadackers, J. Piron-Abellan, V. Shemet and L. Singheiser, *Materials at High Temperatures*, **20**, 115-127 (2003).
4. J. Froitzheim, G. H. Meier, L. Niewolak, P. J. Ennis, H. Hattendorf, L. Singheiser and W. J. Quadackers, *Journal of Power Sources*, **178**, 163-173 (2008).
5. M. Schuisky, A. Rosberg, L. Mikkelsen, S. Linderoth**, N. Christiansen and J. G. Larsen***, in *26th Risø International Symposium on Materials Science: Solid State Electrochemistry*, S. Linderoth, A. Smith, N. Bonanos, A. Hagen, L. Mikkelsen, K. Kammer, D. Lybye, P. V. Hendriksen, F. W. Poulsen, M. Mogensen and W. G. Wang Editors (2005).
6. M. Krumpelt, T. A. Cruse, B. J. Ingram, J. L. Routbort, S. L. Wang, P. A. Salvador and G. Chen, *Journal of the Electrochemical Society*, **157**, B228-B233 (2010).
7. S. P. Jiang and Y. Zhen, *Solid State Ionics*, **179**, 1459-1464 (2008).
8. M. Kornely, A. Neumann, N. H. Menzler, A. Leonide, A. Weber and E. Ivers-Tiffée, *Journal of Power Sources*, **196**, 7203-7208 (2011).
9. N. Yasuda, T. Uehara, M. Okamoto and J. Yamamura, in *European Fuel Cell Forum Lucerne* (2010).
10. N. Birks, G. Meier and F. Petit, *High Temperature Oxidation of Metals*, Cambridge University Press (2009).
11. P. Kofstad, *High Temperature Corrosion*, Elsevier Applied Science Publishers (1988).
12. *High Temperature Oxidation and Corrosion of Metals* (2008).
13. C. S. Tedmon, *Journal of the Electrochemical Society*, **113**, 766-768 (1966).
14. B. B. Ebbinghaus, *Combustion and Flame*, **93**, 119-137 (1993).
15. E. J. Opila, D. L. Myers, N. S. Jacobson, I. M. B. Nielsen, D. F. Johnson, J. K. Olminky and M. D. Allendorf, *Journal of Physical Chemistry A*, **111**, 1971-1980 (2007).
16. J. Froitzheim, H. Ravash, E. Larsson, L. G. Johansson and J. E. Svensson, *Journal of the Electrochemical Society*, **157**, B1295-B1300 (2010).
17. H. Asteman, K. Segerdahl, J. E. Svensson and L. G. Johansson, in *High Temperature Corrosion and Protection of Materials 5, Pts 1 and 2*, R. Streiff, I. G. Wright, R. C. Krutenat, M. Caillet and A. Galerie Editors, p. 277-285 (2001).
18. H. Frenz, *Materials and Corrosion*, **48**, 556-557 (1997).
19. A. B. Stambouli and E. Traversa, *Renewable and Sustainable Energy Reviews*, **6**, 433-455 (2002).
20. Bloom Energy, in (2015).

21. S. C. Singhal and K. Kendall, *High-temperature Solid Oxide Fuel Cells*, p. 1-405, Elsevier Advanced Technology (2003).
22. M. Palcut, L. Mikkelsen, K. Neufeld, M. Chen, R. Knibbe and P. V. Hendriksen, *Corrosion Science*, **52**, 3309-3320 (2010).
23. H. S. Seo, D. W. Yun and K. Y. Kim, *International Journal of Hydrogen Energy*, **38**, 2432-2442 (2013).
24. J. H. Froitzheim, Ferritic steel interconnectors and their interactions with Ni base anodes in solid oxide fuel cells (SOFC), in *04 Fakultät für Maschinenwesen RWTH Aachen* (2008).
25. B. Kuhn, C. A. Jimenez, L. Niewolak, T. Hüttel, T. Beck, H. Hattendorf, L. Singheiser and W. J. Quadackers, *Materials Science and Engineering A*, **528**, 5888-5899 (2011).
26. L. Garcia-Fresnillo, V. Shemet, A. Chyrkin, L. G. J. de Haart and W. J. Quadackers, *Journal of Power Sources*, **271**, 213-222 (2014).
27. L. Niewolak, E. Wessel, T. Huttel, C. Asensio-Jimenez, L. Singheiser and W. J. Quadackers, *Journal of the Electrochemical Society*, **159**, F725-F732 (2012).
28. C. Key, J. Eziashi, J. Froitzheim, R. Amendola, R. Smith and P. Gannon, *Journal of the Electrochemical Society*, **161**, C373-C381 (2014).
29. M. Versluijs, *Department of Chemistry, Group of Inorganic Chemistry and Catalysis, The University of Utrecht, The Netherlands*.
30. C. Hammond, *Journal of Microscopy*, **159**, 123-124 (1990).
31. Y. Mrabet, *Wikipedia*.
32. G. Gauglitz, in *Ullmann's Encyclopedia of Industrial Chemistry*, Wiley-VCH Verlag GmbH & Co. KGaA (2000).
33. P. D. J. Lindner, 2015
34. D. B. Williams and C. B. Carter, *Transmission Electron Microscopy*, Plenum Press, New York (1996).
35. P. J. Schields, 2001
36. S. Fontana, S. Chevalier and G. Caboche, *Journal of Power Sources*, **193**, 136-145 (2009).
37. H. J. Grabke, *Surface and Interface Analysis*, **30**, 112-119 (2000).
38. P. Y. Hou and J. Stringer, *Materials Science and Engineering: A*, **202**, 1-10 (1995).
39. R. W. Jackson, J. P. Leonard, L. Niewolak, W. J. Quadackers, R. Murray, S. Romani, G. J. Tatlock, F. S. Pettit and G. H. Meier, *Oxidation of Metals*, **78**, 197-210 (2012).
40. B. Pieraggi and R. A. Rapp, *Journal of the Electrochemical Society*, **140**, 2844-2850 (1993).
41. B. A. Pint, *Oxidation of Metals*, **45**, 1-37 (1996).
42. H. S. Seo, G. Jin, J. H. Jun, D.-H. Kim and K. Y. Kim, *Journal of Power Sources*, **178**, 1-8 (2008).

43. J. Froitzheim, S. Canovic, M. Nikumaa, R. Sachitanand, L. G. Johansson and J. E. Svensson, *Journal of Power Sources*, **220**, 217-227 (2012).
44. I. H. Jung, *Solid State Ionics*, **177**, 765-777 (2006).
45. L. Kjellqvist and M. Selleby, *Journal of Alloys and Compounds*, **507**, 84-92 (2010).
46. S. Canovic, Unpublished micrographs in, Chalmers University of Technology (2012).
47. H. Al-Badairy, G. J. Tatlock and M. J. Bennett, *Materials at High Temperatures*, **17**, 101-107 (2000).
48. D. P. Whittle, *Corrosion Science*, **12**, 869-872 (1972).
49. M. Stanislawski, E. Wessel, K. Hilpert, T. Markus and L. Singheiser, *Journal of the Electrochemical Society*, **154**, A295-A306 (2007).
50. M. Schütze and D. R. Holmes, *Protective oxide scales and their breakdown*, Wiley, Chichester (1997).
51. L. Niewolak, D. J. Young, H. Hattendorf, L. Singheiser and W. J. Quadackers, *Oxidation of Metals*, **82**, 123-143 (2014).
52. S. P. Jiang, L. Liu, K. P. Ong, P. Wu, J. Li and J. Pu, *Journal of Power Sources*, **176**, 82-89 (2008).
53. N. Sakai, T. Horita, Y. P. Xiong, K. Yamaji, H. Kishimoto, M. E. Brito, H. Yokokawa and T. Maruyama, *Solid State Ionics*, **176**, 681-686 (2005).
54. A. Holt and P. Kofstad, *Solid State Ionics*, **69**, 137-143 (1994).
55. M. Bertoldi, O. Bucheli and A. Ravagni, *ECS Transactions*, **68**, 117-123 (2015).
56. B. P. Borglum and H. Ghezal-Ayagh, *ECS Transactions*, **68**, 89-94 (2015).
57. R. T. Leah, A. Bone, M. Lankin, A. Selcuk, M. Rahman, A. Clare, L. Rees, S. Phillip, S. Mukerjee and M. Selby, *ECS Transactions*, **68**, 95-107 (2015).
58. A. Mai, J. A. Schuler, F. Fleischhauer, V. Nerlich and A. Schuler, *ECS Transactions*, **68**, 109-116 (2015).
59. T. Strohbach, F. Mittmann, C. Walter, D. Schimanke and C. Geipel, *ECS Transactions*, **68**, 125-129 (2015).
60. L. Osaka Gas Co., L. Aisin Seiki Co., K. Corporation, L. Chofu Seisakusho Co. and T. M. Corporation, 2012
61. S. Hardman, A. Chandan and R. Steinberger-Wilckens, *Journal of Power Sources*, **287**, 297-306 (2015).
62. J. G. Grolig, J. Froitzheim and J. E. Svensson, *Journal of Power Sources*, **248**, 1007-1013 (2014).
63. A. Magrasó, H. Falk-Windisch, J. Froitzheim, J. E. Svensson and R. Haugrud, *International Journal of Hydrogen Energy* (2015).
64. J. Tallgren, M. Bianco, O. Himanen, O. Thomann, J. Kiviaho and J. van Herle, *ECS Transactions*, **68**, 1597-1608 (2015).
65. P. Gannon and R. Amendola, *Jom*, **64**, 1470-1476 (2012).